

***Final Draft***  
**of the original manuscript:**

Xia, D.; Huang, G.; Liu, S.; Tang, A.; Gavras, S.; Huang, Y.; Hort, N.; Jiang, B.; Pan, F.:

**Microscopic deformation compatibility during biaxial tension in AZ31 Mg alloy rolled sheet at room temperature.**

In: Materials Science and Engineering: A. Vol. 756 (2019) 1 - 10.

First published online by Elsevier: 10.04.2019

<https://dx.doi.org/10.1016/j.msea.2019.04.029>

# Microscopic deformation compatibility during biaxial tension in AZ31 Mg alloy rolled sheet at room temperature

Dabiao Xia <sup>a,b</sup>, Guangsheng Huang <sup>a,b,c,\*</sup>, Shuaishuai Liu <sup>a,b</sup>, Aitao Tang <sup>a,b,c</sup>, Serge Gavras <sup>d</sup>, Yuanding Huang <sup>d</sup>, Norbert Hort <sup>d</sup>, Bin Jiang <sup>a,b,c\*</sup>, Fusheng Pan <sup>a,b,c</sup>

<sup>a</sup> State Key Laboratory of Mechanical Transmission, College of Materials Science and Engineering, Chongqing University, Chongqing 400044, China

<sup>b</sup> National Engineering Research Center for Magnesium Alloys, Chongqing University, Chongqing 400044, China

<sup>c</sup> Chongqing Research Center for Advanced Materials, Chongqing Academy of Science & Technology, Chongqing 401123, China

<sup>d</sup> MagIC-Magnesium Innovation Centre, Helmholtz-Zentrum Geesthacht, Max-Planck-Str. 1, 21502 Geesthacht, Germany

## Abstract

In this paper, *in situ* electron back scattered diffraction combined with scanning electron microscopy and digital image processing techniques were used to study the microscopic deformation compatibility of AZ31 Mg alloy rolled sheets with strong basal texture during biaxial tension at room temperature. The results firstly quantitatively showed that the distribution of microscopic strain in AZ31 rolled sheet was inhomogeneous during formation. Strain concentrations happened in some regions even at early stage of deformation. Short distorted bands also appeared in these regions and extended to connect each other with increasing macroscopic strain. The appearance of distorted bands play an important role in strain compatibility since the materials lack easy deformation modes at room temperature. Besides slips and twins, the grain distortion should also be an indispensable mechanism in accommodating plastic deformation in some parts in distorted bands. According to the

---

\* Corresponding author: College of Materials Science and Engineering, Chongqing University, Chongqing 400044, China.

E-mail address: gshuang@cqu.edu.cn (G.S. Huang), binjiang@cqu.edu.cn (B. Jiang).

analysis from the Schmid factor, the geometric compatibility factors and slip trace identification, the comprehensive effect of strong basal texture and biaxial tensile stress state not only led to the quite low SFs for prismatic  $\langle a \rangle$ , pyramidal  $\langle a \rangle$  slips and tensile twinning, but limited the compatibility between slip systems and tensile twins. This mechanism was the main reason for the lack of easy deformation modes and the appearance of distorted bands, which further led to the inhomogeneous strain distribution at room temperature. Therefore, the formability of Mg alloys rolled sheets with strong basal texture was weakened at room temperature.

*Key words:* magnesium alloy; deformation compatibility; microstructure; in situ EBSD; basal texture

## **1. Introduction**

In recent years, the applications of magnesium alloys have increased rapidly for automotive, aerospace and communications industries for which weight reduction is highly required [1-4]. The Mg alloy rolled sheets even draw special attention due to their great potential in future applications [5-7]. However, the adoption of Mg alloy rolled sheets remains limited compared with that of steel and aluminum alloys [8-10]. Their poor deformability at room temperature mainly results from their intrinsic hexagonal close packed crystal structure [11-14]. Hence, continuous efforts have been made to improve the formability of Mg alloy rolled sheets and to extend their commercial applications in recent years.

The fundamental challenge to improve the formability of Mg alloy rolled sheet is to activate more deformation modes and improve the compatibilities to coordinate the macroscopic plastic flow. The specific methods include grain coarsening, basal texture randomizing/weakening, alloying and raising the forming temperature, etc. The coarse grains in Mg alloys can significantly enhance the twin formation. The lattice rotation caused by twinning behavior induces the strain in the thickness direction by enhancing the slip activities [15, 16]. In addition, non-basal slip systems will dominate the material flow instead of basal slip with increasing grain size. The compatibilities between different deformation modes are promoted as well [17, 18].

All these improvements can benefit the formability of Mg alloy rolled sheets.

The initial texture can also influence the sheet formability significantly. With specific texture orientation and distribution, the critical resolved shear stress (CRSS) of prismatic slip and twinning are decreased [19, 20]. Similar effects were also achieved by randomizing or weakening the basal texture [21-25]. An effective approach to randomize/ weaken the texture is the utilization of rare earth (RE) elements such as Gd, La, Nd, Ce and Y [12, 26-29]. With RE addition,  $CRSS_{prism}/CRSS_{twinning}$  and  $CRSS_{pyr}/CRSS_{twinning}$  ratios decrease which can improve the activation of prismatic and other non-basal slip systems [30-33]. The results based on visco-plastic self-consistent (VPSC) simulation indicated that the formability of Mg alloys can be efficiently improved with increasing activities of prismatic slips and non-basal slips [34-36]. However, they were mostly obtained based on the theoretical simulations. The actual activation ratios between different deformation modes are still unclear since the practical statistics are difficult to obtain. Moreover, although the accommodation between slips and twins should be important in coordinating plastic strain during formation, the practical observations about the accommodating behaviors on microscopic scales were rarely reported. The slow development of biaxial tension testers is likely to be the main reason for the previous lack of information [37, 38].

*In situ* experimental methods and digital image processing techniques have been well developed in recent years. These techniques can provide a new insight into the evolution of microstructure and microscopic strain distribution in Mg alloys during deformation [20, 39-45]. The *in situ* acoustic emission techniques have been widely used to study the local dislocation activity [46, 47]. With *in situ* SEM experiments, the relative contributions of different slip systems in the Mg alloy AZ31 during uniaxial tensile were proved to be: 41% basal, 44% prismatic  $\langle a \rangle$  and 15% pyramidal  $\langle a+c \rangle$  at 423 K [39]. The *in situ* electron back scattered diffraction (EBSD) results indicated that tensile twin chains were a type of strain compatibility behaviors among twin variants in adjacent grains, rather than twins moving across grain boundaries in

adjacent grains [40]. This effect, in combination with digital image correlation, proved that microscopic strain distribution was significant inhomogeneous in copper, aluminum and Mg alloys during uniaxial tension [48-50]. However, reports about microstructural evolutions for Mg alloys during formation were quite few, especially for the relationship between strain localizations and activities of dislocations obtained from *in situ* experiments [51, 52].

AZ31 rolled sheets were widely used materials, which is often deformed under biaxial tensile stress state (BTSS) during stamping, bending or other complicated forming processes. In the present work, biaxial tension tests for the hot-rolled AZ31 sheets were conducted using a new specific device to study their microstructural evolutions during forming. The new device is simple, cheap and functional for micro biaxial tension tests. The combination of *in situ* EBSD, scanning electron microscopy (SEM) and image processing techniques were firstly used to characterize the microstructural changes as well as the quantitative measurement of microscopic strain distribution in AZ31 rolled sheets during formation.

## **2. Material and methods**

The material in this investigation was a commercial AZ31 Mg alloy hot rolled sheet from Yinguang Magnesium Industry Group Co., LTD. The sheet was then fully recrystallized at 450 °C for 20 min. The high annealing temperature is beneficial for grains to grow up and consequently the formability could be improved as well [15]. In order to investigate the anisotropy of the annealed samples in rolling direction (RD)-transverse direction (TD) plane, the typical tensile tests were conducted using the specimens with a gauge length of 12.5 mm, width of 6 mm and thickness of 0.6 mm. The strain rate was set as  $10^{-3} \text{ s}^{-1}$ .

The samples for biaxial tension testing were prepared by sectioning to the dimensions shown in Fig. 1a and mechanically ground on the RD-TD plane of the sheet. The ground samples were electro-polished using the commercial electrolyte AC II at 0 °C, with a voltage of 20 V for 120 s. The freshly polished sample was set

into the biaxial tension device shown in Fig. 1(b). This device is similar to the equipment used for Erichsen tests except that the sample was held by tightening the nut and the punch was driven by rotating the loading screw (Fig. 1b). The dome height of the sample was equal to the stroke of the punch. According to five pre-tests, the average dome height before fracture was about 1.50 mm. Hence, in the present *in situ* tests, the interrupting punch strokes were selected with 0.12 mm, 0.24 mm, 0.36 mm, 0.48 mm, 0.72 mm, 0.84 mm, 1.08 mm and 1.50 mm (broken).

Automatic *in situ* EBSD measurements were performed using a JEOL JSM 7800F field emission SEM equipped with a HKL Channel 5.0 software using a step size of 0.6  $\mu\text{m}$ . Before deformation, the microstructure of the initial sample's center was measured by EBSD once. In order to calculate the following microscopic strain, micro grids, having a step size of 10  $\mu\text{m}$  and a width of 200  $\mu\text{m}$  [48], were deposited on the EBSD-measured region of the sample using a Zeiss AURIGA SEM-Focused ion beam miller (FIB). After the FIB process, the surface morphology (including the grids) of the sample was captured and saved as high-resolution images using SEM. Then, the whole device was taken out from SEM. The first deformation step was proceeded by rotating the screw to the corresponding degree so that the dome height would be 0.12 mm. The average speed of the punch was about 0.36 mm/min. After deformation, the device was set back into the SEM. The morphology of the deformed sample was imaged again and the EBSD measurement was conducted as well. The subsequent similar steps were carried out in the same way until the fracture of the sample occurred (with 1.50 mm dome height) [51].

The digital image process program was then developed to convert the collected high-resolution images to grayscale, then, count the total pixels in each grid. The total number change of pixels in the grid was treated as the area change of the grid with different dome height. The corresponding microscopic strain  $\varepsilon$  of one grid was calculated using Eq. (1):

$$\varepsilon = \frac{S_i - S_0}{S_0} \quad \text{Eq. (1)}$$

$S_0$  is the initial area of the grid and  $S_i$  is the corresponding area after deformation. This program also gave the gravity center of the grid to assign it the total

microscopic strain in the grid.

### 3. Results

#### 3.1. Initial microstructure and mechanical properties

An EBSD map of the alloy in the initial condition and corresponding texture pole figure are shown in Fig. 2a and b respectively. The rolled sheet exhibits a fully recrystallization microstructure with an average linear intercept grain size of  $\sim 30 \mu\text{m}$ . Some large grains have a size of  $\sim 80 \mu\text{m}$  while some other grains can be as small as  $\sim 15 \mu\text{m}$ . Their influences on plastic deformation may be different. Fig. 2b reveals a strong  $\{0001\}$  basal texture of the sheet. The typical uniaxial tensile true stress-strain curves of the annealed samples are shown in Fig. 2c. It indicates that the curves in three directions are quite close. Hence, the sheet is regarded as isotropic in RD-TD plane in this paper.

#### 3.2 Quantitative investigations on microscopic strain evolution

Fig. 3a ~ h show the microstructural evolution during the biaxial tension superimposed with strain maps. The lines of the grids were marked again to make them clear in Fig. 3 and other subsequent figures. In Fig. 3, the strain maps exhibit inhomogeneous strain distribution. The range of the strain is approximately  $-0.4 \sim 1.2$ . Tensile and compressive strains coexist. The high-level microscopic strains appeared in certain regions even with relatively low dome height of 0.12 mm (Fig. 3a). Their locations were quite stable during formation and hardly changed. With increasing dome height, the strain values in high-strain regions also increase.

The quantitative calculations of the inhomogeneous strain distribution at different strain levels are shown in Fig. 4. Fig. 4a exhibits the normalized strain distribution measured from Fig. 3 at different strain levels. The distribution of local normalized strain is in a range of  $(-1 \sim 7)$ . The fraction of the normalized strain with  $\sim 1$  increases with increasing macroscopic strain. However, the fraction  $\sim 3$  is still notable during the whole formation. This means that the strain concentration always exists. The strain standard deviation at different scale lengths is shown in Fig. 4b. Its

definition was described by Sun et al. [48]. It decreases with the increment of scale length at every strain level. This suggests that the inhomogeneous strain distribution is not in macro-scale (such as shear bands), but rather than at the grain level, similar to that under uniaxial tensile stress state (UTSS) [48].

The morphological evolution of the meshed region is shown in Fig. 5. Slip traces and shear stages began to appear early with 0.12 mm dome height (Fig. 5b1 and b2). Secondary twins are shown to exist in the sheared stages using orientation identification method (Fig. 5b2 and 5b3). The appearance of secondary twins can be attributed to their large matrix grain, which typically causes a stress concentration at grain boundaries. In addition, the short distorted bands (DBs) are observed in some regions as well (Fig. 5b). Due to the fact EBSD measurements are not functional in these bands, the determination that twins are in them or not is not known. With the dome heights increasing to 1.50 mm (broken), the DBs extend to connect each other (Fig. 5c). The concentration of secondary twins has given rise to the occurrence of a micro crack. This crack is numbered as crack-1, as depicted in Fig. 5c. Fig. 5d presents that shear bands exist in RD-normal direction (ND) plane after fracture. The angle between RD-TD plane and shear bands is  $\pm \sim 30^\circ$ , which is typical for AZ31 rolled sheet with a strong basal texture [53].

## 4. Discussion

### 4.1. Evolution of microscopic strain distribution

Since the microscopic strain is inhomogeneous, the strain rate in different regions should be inhomogeneous as well. It was reported that both the activation of deformation modes and the strain hardening effect in Mg alloys are sensitive to the strain rate [54]. In the present work, the speed of the punch is an estimated average value. The strain rate at the center of the sample is not linearly related with the speed of punch. Hence, the distribution of the strain evolution standard deviation ( $S_{SE}$ ) instead of the true strain rate is calculated for each grid in the meshed region during the biaxial tension. The definition of  $S_{SE}$  is introduced as Eq. (2):

$$S_{SE} = \sqrt{\frac{1}{N} \sum_{i=1}^N (\varepsilon_e - \bar{\varepsilon}_e)^2}$$

Eq. (2)

$\varepsilon_e$  is one measured strain value of one grid,  $\bar{\varepsilon}_e$  the average strain of this grid during the whole deformation and  $N$  is the total number of the measured strain values.

As an index of one grid's strain fluctuation,  $S_{SE}$  can qualitatively represent the average strain rate of the grid. The calculation results (Fig. 6a) suggest that not only these regions with intermediate-level strains but also some grids with intermediate-level strains have a high  $S_{SE}$ . Normally, DBs and micro cracks prefer to form in those grids with high  $S_{SE}$ , rather than with high-level strains (Fig. 6b). It can then be concluded that the appearance of DBs should contribute to the high strain rate, instead of high-level strain. The fracture may occur along these DBs owing to the stronger strain strengthening caused by the high strain rate if the friction between the punch and the sample is zero.

Fig. 6a also indicates that the highest  $S_{SE}$  appears near crack-1, not in DBs. After numbering all the grids in Fig. 6a, the microscopic strain evolutions of some grids with high  $S_{SE}$  near crack-1 are shown in Fig. 6c and those in DBs are shown in Fig. 6d. Most grids in Fig. 6c have a fluctuating strain evolution while the strains of most grids in Fig. 6d increase monotonically. The highest  $S_{SE}$  should be caused by the fluctuating strain. Since the secondary twins are continuously concentrated near the crack-1, it can be easily inferred that the shear strain caused by secondary twins should be the main reason for the fluctuating strain in Fig. 6c. That is to say, the high strain rate caused by secondary twin should be an important mechanism responsible for the fracture in Mg alloys [55]. In general, a possible way to prevent Mg alloy rolled sheets from prematurely fracturing is by inhibiting the high-level strain rate caused by the inhomogeneity of strain distribution.

#### 4.2. Relationship between SF and microscopic strain

From Fig. 3 and Fig. 6, it can be found that most regions with high-level strain or high strain rate are distributed in DBs. It can thus be inferred that the appearance of DBs is an important mode for strain accommodation. As it is well known, in sheets

for one deformation mode with large value of SF, a lower applied stress is required to activate its operation and its deformation becomes easier to be coordinated as well [56]. Firstly, the relationship between DBs and SFs of five important modes in Mg alloys were investigated. The calculation method for SF under different stress states was introduced from Xia *et al.* [51]. The results are shown in Fig. 7. It indicates that the SFs for prismatic  $\langle a \rangle$  and tensile twinning are quite low. The SF for basal  $\langle a \rangle$  is also not much higher. Even though the SF for pyramidal  $\langle a+c \rangle$  is high, its contribution to deformation should be ignored due to the very high critical resolved shear stresses (CRSS) [13, 57, 58]. Compared with Fig. 6b and Fig. 7, however, it seems that there is no clear relationship between SFs and DBs. This infers that the appearance of DBs and their gradually joining together with increasing dome height may not be or may not only be dominated by SF.

It is notable that most of the SFs under BTSS are quite low, especially for prismatic  $\langle a \rangle$  and tensile twinning. The SFs for the same five deformation modes under UTSS were calculated as a comparison (Fig. 8). The loading direction is along RD. The SFs for prismatic  $\langle a \rangle$ , pyramidal  $\langle a \rangle$  and tensile twinning under UTSS are much higher than those under BTSS. The activation for these three modes are much harder under BTSS. Mg alloys are well known for having a lack of easy deformation modes at room temperature, even under uniaxial stress state. In the present investigation, the lack of deformation modes should be more serious. The inhomogeneous strain distribution should also be partly influenced by such “hardening” caused by low SFs.

#### 4.3. Deformation compatibility in DBs

The strain compatibility offered by DBs should depend on the local strain compatibility in themselves. To study the local strain compatibility in DBs, the compatibility factors ( $m'$ ) was employed [59, 60]. The microstructures and morphological evolutions of three different representative regions in DBs are presented in Fig. 9-11. Since just basal  $\langle a \rangle$  and prismatic  $\langle a \rangle$  slip traces were observed, all their possible orientations for the studied grains are listed in Fig. 9-11 as

well [17]. The corresponding SFs and  $m'$  values for the investigated grains in Fig. 9-11 are listed in Tab. 1-3.

In Fig. 9, a total of seven grains are present in the region covered by the micrograph. Only basal  $\langle a \rangle$  slip traces were observed in both grains A and D with 0.12 mm dome height. No twins were identified by EBSD. Tab. 1 suggests that the corresponding SFs and  $m'$  values for these two grains are relatively higher than others. With the dome height increasing to 0.84 mm, the short prismatic  $\langle a \rangle$  slip traces appear in grain E. However, both the corresponding SF and  $m'$  values for the prismatic  $\langle a \rangle$  in grain E are relatively low (Tab. 1). It can be inferred that the activation of prismatic  $\langle a \rangle$  in grain E should be related to the high-level local stress. More importantly, “grain distortions” appear in grains B, E and F, which are free of slip traces during the whole tension (Fig. 9). The high-level strains are also concentrated in those grids with grain distortions. The morphology of the folds in grain F are similar to kink bands reported in the previous papers [61, 62]. In kink bands, non-basal slip is the dominant deformation mode. Since EBSD measurement was not available in these DBs, the stress concentration should be high. In these “grain distortions”, non-basal slip, contraction twins or secondary twins should be involved. All these phenomena suggest that the deformation compatibility in these regions is poor.

As a comparison, in Fig. 10, the basal traces appear in grains H, J and K with 0.12 mm dome height. Their corresponding SFs and  $m'$  values are much higher than the other five grains (Tab. 2). In addition, the short prismatic traces are observed in grains L and M. The SFs for their prismatic  $\langle a \rangle$  are low but their  $m'$  values are high. Tensile twins are found in grain N as well. With the dome height increasing to 0.84 mm (0.138 macroscopic strain), several shear ledges are found in grain J. The micro strains are higher in these grids crossed by the shear ledges. According to the identification in Fig. 5b2 and b3, it can be concluded that the secondary twins should also exist in these shear ledges (Fig. 10). The stress level here is higher than other parts. However, the SFs and  $m'$  values in Tab. 2 are higher than those in Tab. 1. No

grain distortion is found in this region and the strain distribution is a little more homogeneous as well. All these phenomena suggest that the deformation compatibility here is better than that in Fig. 10.

In Fig. 11, approximately seven of the eight grains are full of slip traces with 0.12 mm dome height. Most of matrix in grain P is occupied with tensile twins. Basal traces are found in the tensile twins. The corresponding SFs or  $m'$  values in Tab. 3 are higher than those in Tab. 2 and much higher than those in Tab. 1. It should be noted that the  $m'$  between tensile twin and basal slip is theoretically maximum at 0.46 in grain F in Tab. 3. Besides, the SF of tensile twin in grain P is the SF for the activated variant, so is the  $m'$ . With the dome height increasing to 0.84 mm, the basal traces can be observed in every grain, especially for the tensile twins. Since the strain of most grains is high, the micro cracks appear at grain boundaries. A grain distortion is observed at the boundary between grains J and Q as well. There should be no secondary twins since no shear ledges are observed in Fig. 11. The stress level may be lower than that in Fig. 10 or Fig. 9. Hence, the deformation accommodation in Fig. 11 should be the best among these three regions.

For slip-dominated deformation, strain localization at the *inter-granular* scale is located at the place where both  $m'$  values and high SFs for certain deformation modes in adjacent grains should be met under uniaxial stress state [63]. A low  $m'$  value usually leads to a high boundary obstacle effect [64]. However, no matter how good the compatibility is in these regions, DBs (or high-level strains) still concentrate in these regions and offer important strain compatibility for deformation. The distribution of DBs or inhomogeneous strains should not result from good or poor deformation compatibility in grains.

#### 4.4. Influences of stress state and texture on microscopic strain distribution

A strong basal texture can lead to a lack of easy deformation modes in Mg alloys at room temperature. Chun *et al.* [53] reported that with a strong basal texture, more pronounced shear bands appeared in Mg alloys during rolling due to the lack of deformation modes. The formability of Mg alloy rolled sheets also decreased with a

stronger basal texture at room temperature. The mechanism is that a limited amount of prismatic  $\langle a \rangle$  slip was activated in a strong basal texture, further leading to an increase of shear bands [20]. In the present investigation, strong basal texture also exists (Fig. 2b) and shear bands are observed (Fig. 5d). Most of the observed traces are identified as the basal slip as shown in Tab. 4 in which the total number of grains in meshed regions are 244 and traces of other kinds of slip models are not found. The grains with the presence of prismatic slip increases slowly from 2 to 8 with dome height increasing from 0.12 mm to 0.84 mm. The prismatic slip traces are much less than basal traces during the entire deformation. Non-basal slip traces are rarely observed. Yin *et al.* [65] listed all three reasons for the absence of slip traces: (1) the amount of mobile dislocations was not large enough to form an obvious slip trace, (2) the Burgers vector of the dislocation was parallel to the sample surface, and (3) the dislocation did not move to the sample surface. In the present work, the main reasons for very few prismatic  $\langle a \rangle$  or non-basal slip traces should be reason (1). Hence, basal slip should always be the main deformation mode, which offers the most deformation accommodation during deformation under BTSS. There is a lack of easy deformation modes in AZ31 rolled sheets during forming at room temperature. In this case, the stress rapidly concentrates in some regions, which finally causes grain distortion or DBs. This phenomenon should belong to a kind of inhomogeneous geometric texture softening [53].

With the same strong texture, the SFs in Fig. 8 under UTSS are much higher than those in Fig. 7 under BTSS. The deformability for Mg alloys under UTSS is better than that under BTSS [51]. The strong basal texture is not the only reason for the lack of easy deformation modes or for the inhomogeneous strain distribution. The previous works [51] have proved that the BTSS dominated the distribution of SF on (0001) pole figure. The SFs for prismatic  $\langle a \rangle$ , pyramidal  $\langle a \rangle$  and tensile twinning rapidly reduces when two conditions are simultaneously satisfied: (i) Mg alloy sheet is under BTSS in plane; (ii) the intensity of the basal texture is high (both satisfied in this paper). In addition, the accommodations between tensile twins and prismatic  $\langle a \rangle$ ,

pyramidal  $\langle a \rangle$  and tensile twinning are also deteriorated because of BTSS. More importantly; the BTSS can even lead to a higher tangent modulus, which is significant higher than that under UTSS. The strain hardening in Mg alloys is different under BTSS as well [66, 67]. The deformation stress is much higher under BTSS than that under UTSS. This may lead to the increase of stress or strain concentration level. Hence, the BTSS should also be an important reason responsible for the inhomogeneous strain distribution. Therefore, if it is not possible to weaken the strong basal texture, the BTSS should be adjusted to obtain a better formability of Mg alloy rolled sheets. A method to adjust the stress state during formation of Mg alloy rolled sheets is currently being investigated.

## 5. Conclusion

In this paper, *in situ* biaxial tension in SEM combined with EBSD and a digital image processing techniques were applied to quantitatively investigate the forming behavior of Mg alloy rolled sheets with strong basal texture at room temperature.

The following conclusions were made:

- (1) The distribution of microscopic strain in AZ31 rolled sheet is quite inhomogeneous during forming at room temperature. The micro strain distribution under BTSS is more inhomogeneous than that under UTSS. This inhomogeneity of strain is not in the macro-scale, but at grain level. The deformability is limited by the inhomogeneity of strain distribution.
- (2) The formation of DBs is an important mode for strain compatibility. The compatibility between different deformation modes in DBs could be good, poor or intermediary. It is primarily due to the corresponding SFs for the activated modes in the adjacent grains. However, the strain rate in DBs is always higher than other regions.
- (3) In the regions with poor compatibility, the activation of the easiest modes (basal  $\langle a \rangle$ , prismatic  $\langle a \rangle$  and tensile twinning) are limited. In this case, the “grain distortion” resulted from the high-level stress concentration, which plays an

important role in accommodating deformation. However, the grain distortions are often accompanied by micro cracks, which may lead to fracture. Hence, creating grain distortions should be avoided in order to improve the formability of Mg alloy sheets.

- (4) By limiting the SFs for deformation modes and the compatibility between slips and twinning, both the strong basal texture and the BTSS are the main reasons for the lack of easy deformation modes. They further cause the formation of DBs or inhomogeneous strain distribution in AZ31 rolled sheet. Hence, Mg alloy sheets with strong basal texture deform under BTSS during formation should be avoided.

### **Acknowledgements**

This work was supported by The National Key Research and Development Plan (2017YFB1300700), The National Natural Science Foundation of China (No. 51671041, NO. 51531002 and NO. U1764253) and Natural Science Foundation of Chongqing (cstc2017jcyjBX0040). The China Scholarship Council is also gratefully acknowledged for financial support for Dabiao Xia (201806050045).

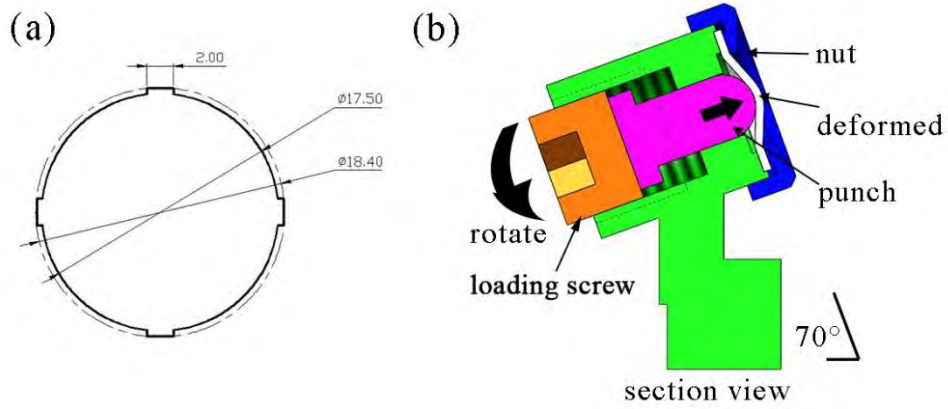


Fig. 1. (a) Dimensions of samples for biaxial tension and (b) schematic of micro biaxial tension system for in-situ EBSD.

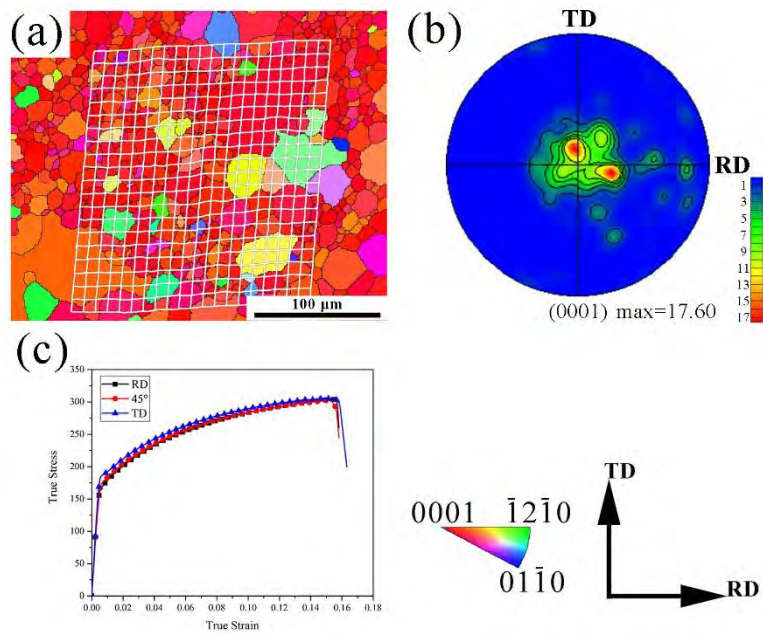


Fig. 2. (a) Initial microstructure, (b) (0001) pole figure and (c) typical uniaxial tensile true stress-strain curves for the annealed AZ31 alloy sheet along RD, TD and 45 °. The grids in (a) were superimposed to show their position.

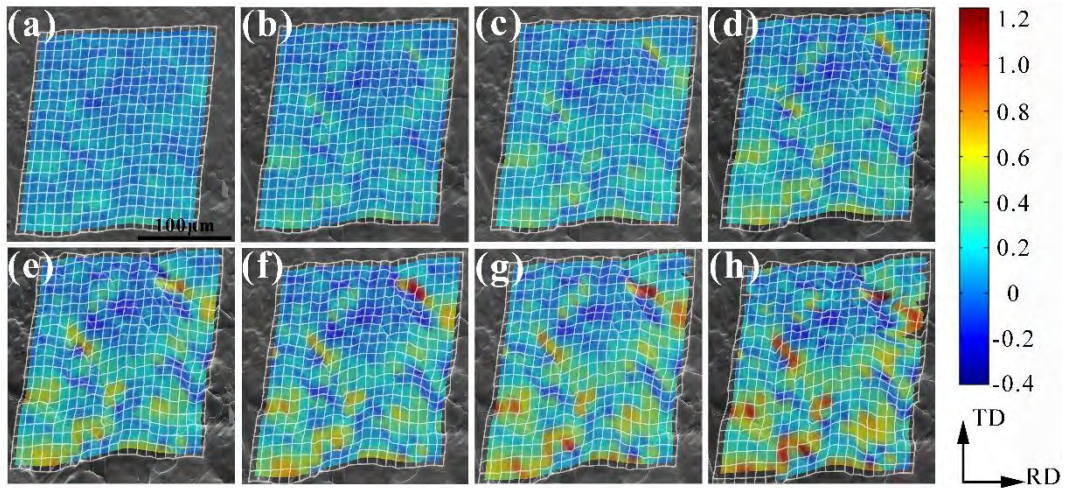


Fig. 3. Strain evolution maps (a) 0.12, (b) 0.24, (c) 0.36, (d) 0.48, (e) 0.72, (f) 0.84, (g) 1.08 and (h) 1.50 mm dome height.

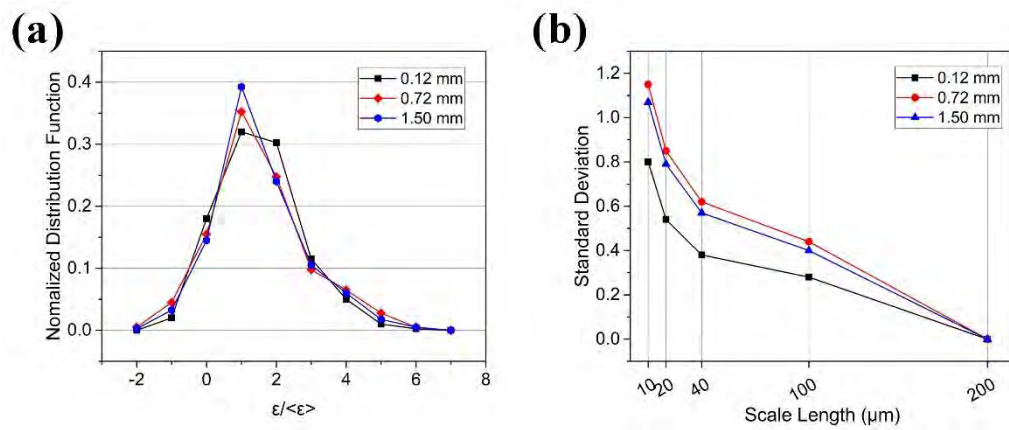


Fig. 4. (a) Normalized strain distribution and (b) standard deviation of strain as a function of scale length at different strain levels ( $\epsilon$  is the measured strain of every grid and  $\langle \epsilon \rangle$  is the average strain of the entire meshed region).

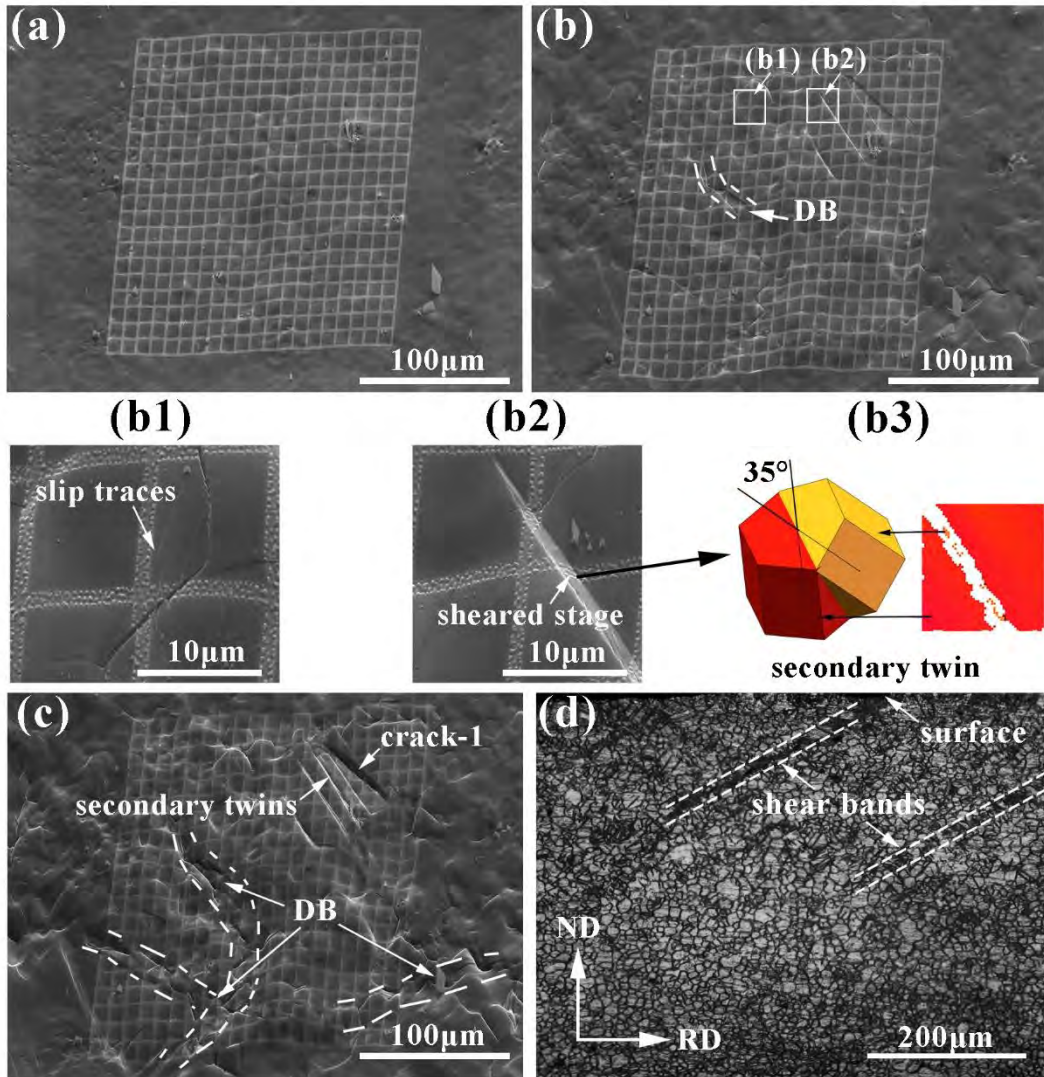


Fig. 5. Morphological evolution with (a) 0 mm, (b) 0.12 mm, (c) 1.50 mm and (d) the microstructure in RD-ND plane with 1.50 mm dome height. At the top of (d) is the measured surface of the sample.

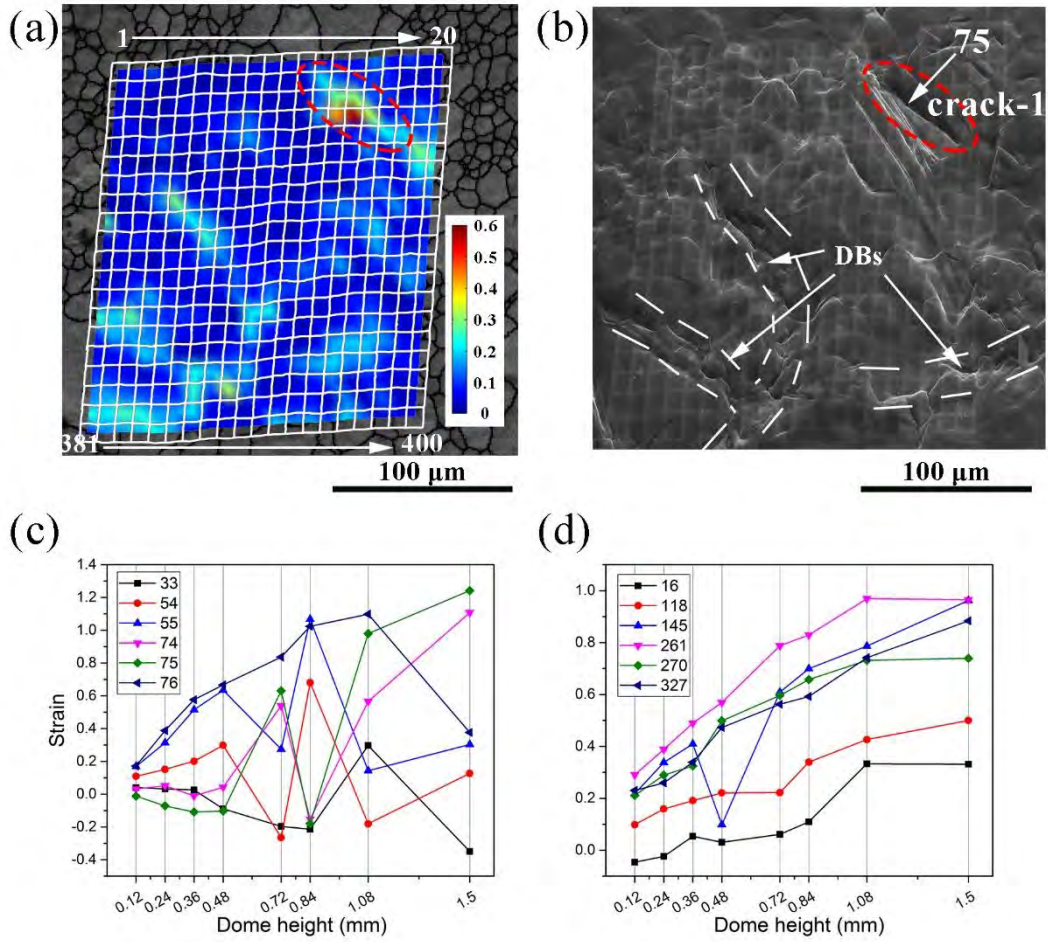


Fig. 6. (a) Distribution of  $S_{SE}$  with gird numbers, (b) the shear bands and microscopic cracks appeared when the dome height was 1.08 mm, “75” is the gird number, (c) the fluctuant strain of some grids and (d) the monotonic increasing strain of some grids.

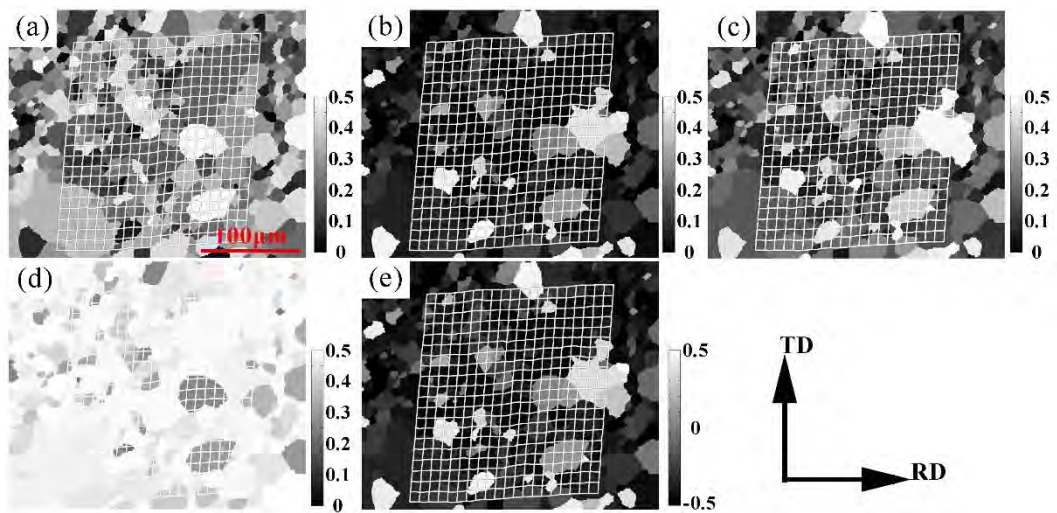


Fig. 7. Distribution of SF for (a) basal  $\langle a \rangle$ , (b) prismatic  $\langle a \rangle$ , (c) pyramidal  $\langle a \rangle$ , (d) pyramidal  $\langle a+c \rangle$  and (e) tensile twinning under BTSS.

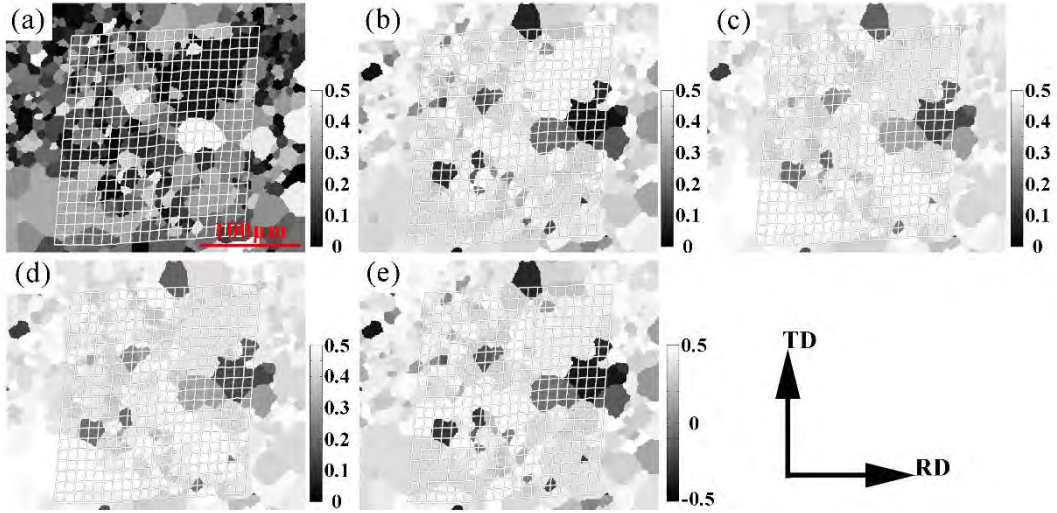


Fig. 8. Distribution of SF for (a) basal  $\langle a \rangle$ , (b) prismatic  $\langle a \rangle$ , (c) pyramidal  $\langle a \rangle$ , (d) pyramidal  $\langle a+c \rangle$  and (e) tensile twinning under UTSS with loading along RD.

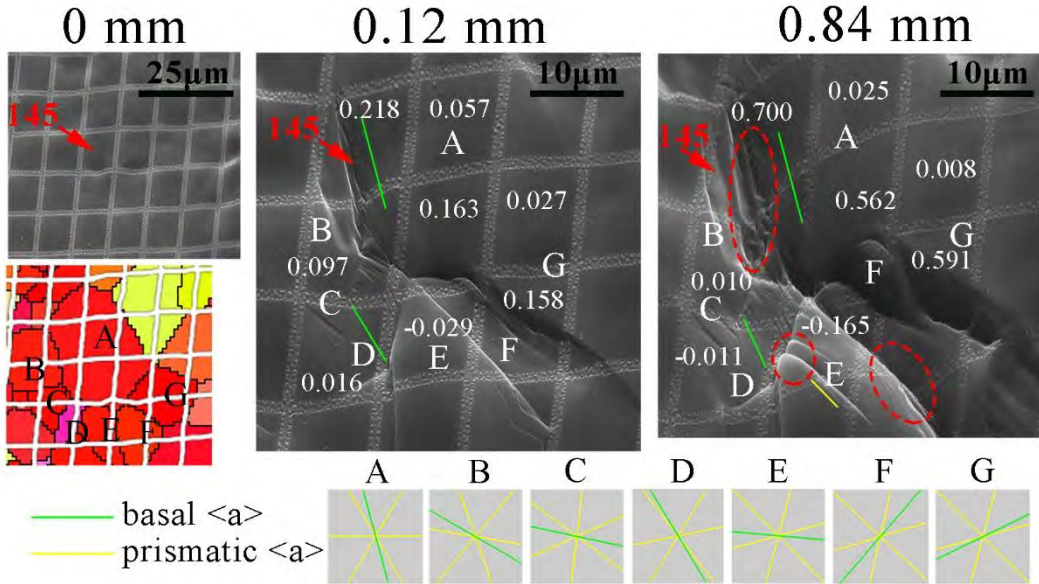


Fig. 9. Microstructural and morphological evolutions of a region in DBs with increasing dome height. Distorted grains are highlighted using red dotted ellipse. The white numbers are the corresponding strains of the grids with corresponding dome height and the number of special grids is also indicated by arrows (similarly hereinafter).

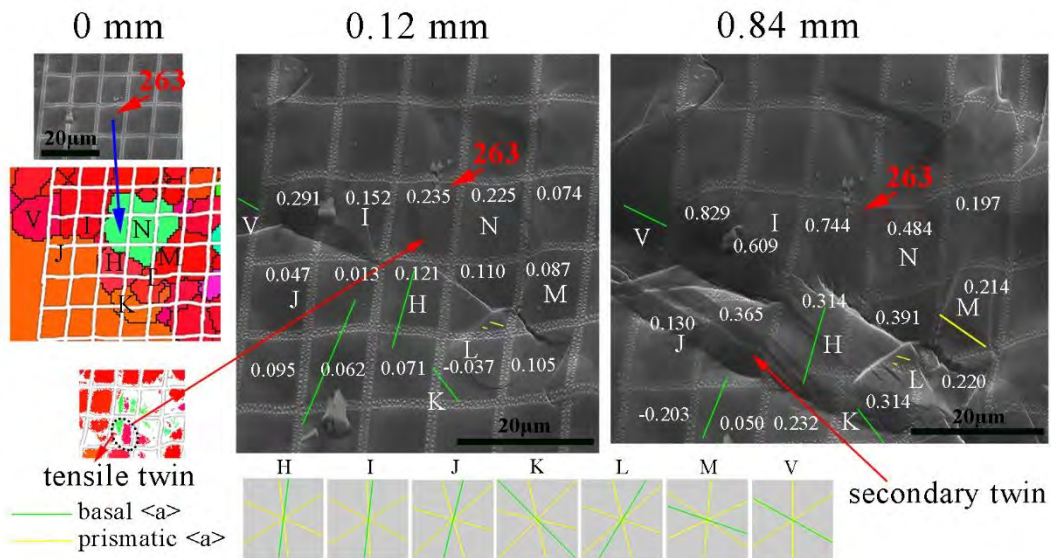


Fig.10. Microstructural and morphological evolutions of a region in DBs including tensile twins and secondary twins with increasing dome height to 0.84 mm.

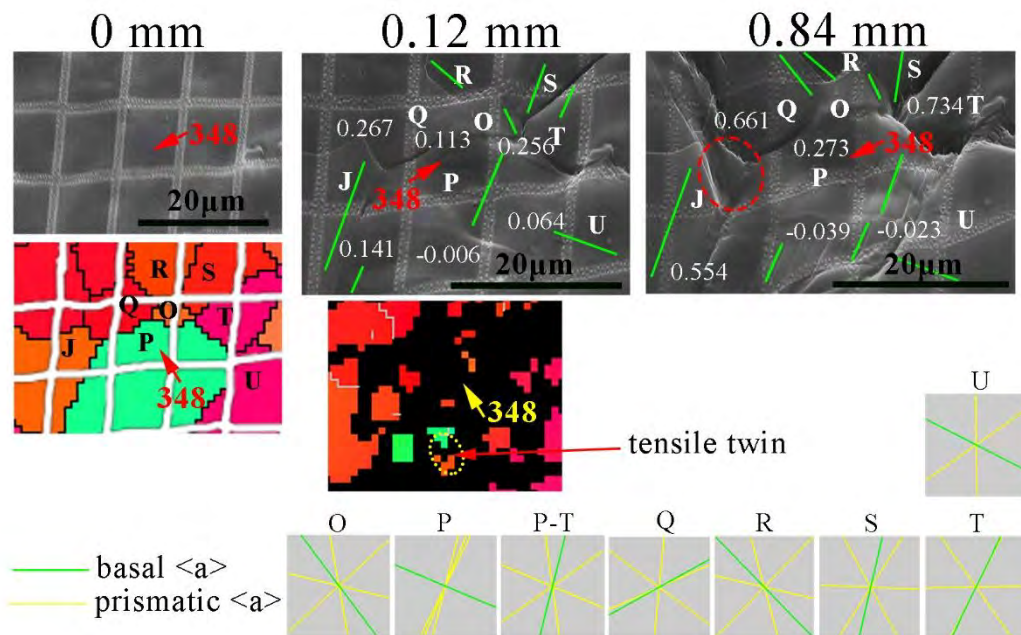


Fig. 11. Microstructural and morphological evolutions of a region in DBs including tensile twins with increasing dome height. Distorted grains are highlighted using dotted ellipse.

Tab. 1 Statistical results of SFs and  $m'$  of grains in Fig. 9.

	SF	$m'$					
		B	C	D	E	F	G
A <i>basal &lt;a&gt;</i>	0.18	<b><i>0.92*</i></b>	<b><i>0.89*</i></b>	0.61	0.27	<b><i>0.94*</i></b>	<b><i>0.95*</i></b>
B <i>basal &lt;a&gt;</i>	<b><i>0.18*</i></b>		<b><i>0.89*</i></b>				
C <i>basal &lt;a&gt;</i>	<b><i>0.08*</i></b>			<b><i>0.74*</i></b>			
D <i>basal &lt;a&gt;</i>	0.45				0.53*		
E <i>prismatic &lt;a&gt;</i>	0.01					<b><i>0.13*</i></b>	
F <i>basal &lt;a&gt;</i>	<b><i>0.17*</i></b>						<b><i>0.99*</i></b>
G <i>basal &lt;a&gt;</i>	<b><i>0.03*</i></b>						

\*As no slip traces are observed in grain B, C, F and G, we use their basal <a> slips to calculate responding SFs and  $m'$  and their results are highlighted using bold italics as a reference since they are not activated (the same below).

Tab. 2 Statistical results of SFs and  $m'$  of grains in Fig. 10

	SF	$m'$					
		I	J	K	L	M	N
H basal $\langle a \rangle$	0.36	0.83*	0.98	0.93	0.17		0.73
I basal $\langle a \rangle$	0.13*		0.83*				0.46*
J basal $\langle a \rangle$	0.36			0.78			
K basal $\langle a \rangle$	0.36				0.30		
L prismatic $\langle a \rangle$	0.02					0.88	
M prismatic $\langle a \rangle$	0.007						0.47
N tensile twin	0.42						
V basal $\langle a \rangle$	0.27	0.95*	0.82				

Tab. 3 Statistical results of SFs and  $m'$  of grains in Fig. 11

	SF	$m'$						
		P	J	Q	R	S	T	U
O basal $\langle a \rangle$	0.41	0.70		0.15		0.01	0.02	
P tensile twin	0.42		0.46	0.32			0.38	0.78
J basal $\langle a \rangle$	0.35			0.90				
Q basal $\langle a \rangle$	0.15				0.89			
R basal $\langle a \rangle$	0.25					0.95		
S basal $\langle a \rangle$	0.20						0.82	
T basal $\langle a \rangle$	0.31							0.77
U basal $\langle a \rangle$	0.32							

Tab. 4 Number of grains in which slip traces appear with different dome height.

	0.12 mm	0.36 mm	0.84 mm
Basal <a>	60	81	85
Prismatic <a>	2	5	8

## Reference

- [1] T.B. Abbott, Magnesium: Industrial and Research Developments Over the Last 15 Years, *Corrosion-Us* 71(2) (2015) 120-127.
- [2] Q.H. Wang, J.F. Song, B. Jiang, A.T. Tang, Y.F. Chai, T.H. Yang, G.S. Huang, F.S. Pan, An investigation on microstructure, texture and formability of AZ31 sheet processed by asymmetric porthole die extrusion, *Mat Sci Eng a-Struct* 720 (2018) 85-97.
- [3] W.J. Joost, P.E. Krajewski, Towards magnesium alloys for high-volume automotive applications, *Scripta Materialia* 128 (2017) 107-112.
- [4] M. Yeganeh, N. Mohammadi, Superhydrophobic surface of Mg alloys: A review, *J Magnes Alloy* 6(1) (2018) 59-70.
- [5] S.H. You, Y.D. Huang, K.U. Kainer, N. Hort, Recent research and developments on wrought magnesium alloys, *J Magnes Alloy* 5(3) (2017) 239-253.
- [6] L.Z. Liu, X.H. Chen, F.S. Pan, A.T. Tang, X.L. Wang, J. Liu, S.Y. Gao, Microstructure, texture, mechanical properties and electromagnetic shielding effectiveness of Mg-Zn-Zr-Ce alloys, *Mat Sci Eng a-Struct* 669 (2016) 259-268.
- [7] W.H. Liu, X. Liu, C.P. Tang, W. Yao, Y. Xiao, X.H. Liu, Microstructure and texture evolution in LZ91 magnesium alloy during cold rolling, *J Magnes Alloy* 6(1) (2018) 77-82.
- [8] J. Kim, H. Ryou, D. Kim, D. Kim, W. Lee, S.H. Hong, K. Chung, Constitutive law for AZ31B Mg alloy sheets and finite element simulation for three-point bending, *Int J Mech Sci* 50(10-11) (2008) 1510-1518.
- [9] J.H. Zhang, S.J. Liu, R.Z. Wu, L.G. Hou, M.L. Zhang, Recent developments in high-strength Mg-RE-based alloys: Focusing on Mg-Gd and Mg-Y systems, *J Magnes Alloy* 6(3) (2018) 277-291.
- [10] L.L.C. Catorceno, H.F.G. de Abreu, A.F. Padilha, Effects of cold and warm cross-rolling on microstructure and texture evolution of AZ31B magnesium alloy sheet, *J Magnes Alloy* 6(2) (2018) 121-133.
- [11] M.H. Yoo, Slip, Twinning, and Fracture in Hexagonal Close-Packed Metals, *Metall Trans A* 12(3) (1981) 409-418.
- [12] K. Hantzsche, J. Bohlen, J. Wendt, K.U. Kainer, S.B. Yi, D. Letzig, Effect of rare earth additions on microstructure and texture development of magnesium alloy sheets, *Scripta Materialia* 63(7) (2010) 725-730.
- [13] R.E. Reedhill, W.D. Robertson, Additional Modes of Deformation Twinning in Magnesium, *Acta Metall Mater* 5(12) (1957) 717-727.
- [14] Z. Keshavarz, M.R. Barnett, EBSD analysis of deformation modes in Mg-3Al-1Zn, *Scripta Materialia* 55(10) (2006) 915-918.
- [15] Y. Chino, K. Kimura, M. Mabuchi, Deformation characteristics at room temperature under biaxial tensile stress in textured AZ31 Mg alloy sheets, *Acta Mater* 57(5) (2009) 1476-1485.
- [16] M.R. Barnett, A rationale for the strong dependence of mechanical twinning on grain size, *Scripta Materialia* 59(7) (2008) 696-698.
- [17] C.M. Cepeda-Jimenez, J.M. Molina-Aldareguia, M.T. Perez-Prado, Effect of grain size on slip activity in pure magnesium polycrystals, *Acta Mater* 84 (2015)

443-456.

- [18] Q. Yu, L. Qi, R.K. Mishra, J. Li, A.M. Minor, Reducing deformation anisotropy to achieve ultrahigh strength and ductility in Mg at the nanoscale, *P Natl Acad Sci USA* 110(33) (2013) 13289-13293.
- [19] T. Al-Samman, G. Gottstein, Room temperature formability of a magnesium AZ31 alloy: Examining the role of texture on the deformation mechanisms, *Mat Sci Eng a-Struct* 488(1-2) (2008) 406-414.
- [20] H.L. Kim, W.K. Bang, Y.W. Chang, Effect of initial texture on deformation behavior of AZ31 magnesium alloy sheets under biaxial loading, *Mat Sci Eng a-Struct* 552 (2012) 245-251.
- [21] Y. Chino, K. Sassa, A. Kamiya, M. Mabuchi, Enhanced formability at elevated temperature of a cross-rolled magnesium alloy sheet, *Mat Sci Eng a-Struct* 441(1-2) (2006) 349-356.
- [22] X.S. Huang, K. Suzuki, Y. Chino, Influences of initial texture on microstructure and stretch formability of Mg-3Al-1Zn alloy sheet obtained by a combination of high temperature and subsequent warm rolling, *Scripta Materialia* 63(4) (2010) 395-398.
- [23] X.S. Huang, K. Suzuki, Y. Chino, M. Mabuchi, Improvement of stretch formability of Mg-3Al-1Zn alloy sheet by high temperature rolling at finishing pass, *Journal of Alloys and Compounds* 509(28) (2011) 7579-7584.
- [24] Y. Chino, M. Mabuchi, Enhanced stretch formability of Mg-Al-Zn alloy sheets rolled at high temperature (723 K), *Scripta Materialia* 60(6) (2009) 447-450.
- [25] A. Vinogradov, V.N. Serebryany, S.V. Dobatkin, Tailoring Microstructure and Properties of Fine Grained Magnesium Alloys by Severe Plastic Deformation, *Adv Eng Mater* 20(4) (2018).
- [26] B.C. Suh, J.H. Kim, J.H. Bae, J.H. Hwang, M.S. Shim, N.J. Kim, Effect of Sn addition on the microstructure and deformation behavior of Mg-3Al alloy, *Acta Materialia* 124 (2017) 268-279.
- [27] B.C. Suh, J.H. Kim, J.H. Hwang, M.S. Shim, N.J. Kim, Twinning-mediated formability in Mg alloys, *Sci Rep-Uk* 6 (2016).
- [28] A. Imandoust, C.D. Barrett, T. Al-Samman, K.A. Inal, H. El Kadiri, A review on the effect of rare-earth elements on texture evolution during processing of magnesium alloys, *J Mater Sci* 52(1) (2017) 1-29.
- [29] T. Al-Samman, X. Li, Sheet texture modification in magnesium-based alloys by selective rare earth alloying, *Mat Sci Eng a-Struct* 528(10-11) (2011) 3809-3822.
- [30] V. Herrera-Solaz, J. LLorca, E. Dogan, I. Karaman, J. Segurado, An inverse optimization strategy to determine single crystal mechanical behavior from polycrystal tests: Application to AZ31 Mg alloy, *International Journal of Plasticity* 57 (2014) 1-15.
- [31] V. Herrera-Solaz, R. Hidalgo-Manrique, M.T. Perez-Prado, D. Letzig, J. Llorca, J. Segurado, Effect of rare earth additions on the critical resolved shear stresses of magnesium alloys, *Mater Lett* 128 (2014) 199-203.
- [32] A. Imandoust, C.D. Barrett, H. El Kadiri, Effect of rare earth addition on  $\{10\overline{1}0\}$  twinning induced hardening in magnesium, *Mat Sci Eng a-Struct* 720 (2018) 225-230.

- [33] P. Hidalgo-Manrique, J.D. Robson, M.T. Perez-Prado, Precipitation strengthening and reversed yield stress asymmetry in Mg alloys containing rare-earth elements: A quantitative study, *Acta Materialia* 124 (2017) 456-467.
- [34] B.-C. Suh, J.H. Kim, J.H. Bae, J.H. Hwang, M.-S. Shim, N.J. Kim, Effect of Sn addition on the microstructure and deformation behavior of Mg-3Al alloy, *Acta Materialia* 124 (2017) 268-279.
- [35] T. Hama, H. Takuda, Crystal plasticity finite-element simulation of work-hardening behavior in a magnesium alloy sheet under biaxial tension, *Computational Materials Science* 51(1) (2012) 156-164.
- [36] S.J. Park, H.C. Jung, K.S. Shin, Analysis of the solidification and deformation behaviors of twin roll cast Mg-6Al-X alloys, *Met Mater Int* 22(6) (2016) 1055-1064.
- [37] Y. Yu, M. Wan, X.D. Wu, X.B. Zhou, Design of a cruciform biaxial tensile specimen for limit strain analysis by FEM, *Journal of Materials Processing Technology* 123(1) (2002) 67-70.
- [38] M. Geiger, W. Hussnatter, M. Merklein, Specimen for a novel concept of the biaxial tension test, *Journal of Materials Processing Technology* 167(2-3) (2005) 177-183.
- [39] C.J. Boehlert, Z. Chen, I. Gutierrez-Urrutia, J. Llorca, M.T. Perez-Prado, In situ analysis of the tensile and tensile-creep deformation mechanisms in rolled AZ31, *Acta Materialia* 60(4) (2012) 1889-1904.
- [40] D.F. Shi, T.M. Liu, T.Y. Wang, D.W. Hou, S.Q. Zhao, S. Hussain, {10-12} Twins across twin boundaries traced by in situ EBSD, *Journal of Alloys and Compounds* 690 (2017) 699-706.
- [41] C.C. Tasan, J.P.M. Hoefnagels, M. Diehl, D. Yan, F. Roters, D. Raabe, Strain localization and damage in dual phase steels investigated by coupled in-situ deformation experiments and crystal plasticity simulations, *International Journal of Plasticity* 63 (2014) 198-210.
- [42] A. Chakkedath, C. Boehlert, D. Hernandez, J. Bohlen, S.B. Yi, D. Letzig, In-Situ Ebsd Technique Characterizes Microstructure Evolution of Magnesium Alloy, *Adv Mater Process* 174(6) (2016) 19-21.
- [43] C. Mo, A. Kontsos, Twinning contributions to strain localizations in magnesium alloys, *Mat Sci Eng a-Struct* 722 (2018) 206-215.
- [44] Y.J. Cui, Y.P. Li, Z.C. Wang, Q. Lei, Y. Koizumi, A. Chiba, Regulating twin boundary mobility by annealing in magnesium and its alloys, *International Journal of Plasticity* 99 (2017) 1-18.
- [45] B.L. Wu, G.S. Duan, X.H. Du, L.H. Song, Y.D. Zhang, M.J. Philippe, C. Esling, In situ investigation of extension twinning-detwinning and its effect on the mechanical behavior of AZ31B magnesium alloy, *Materials & Design* 132 (2017) 57-65.
- [46] A. Vinogradov, A.V. Danyuk, D.L. Merson, I.S. Yasnikov, Probing elementary dislocation mechanisms of local plastic deformation by the advanced acoustic emission technique, *Scripta Mater* 151 (2018) 53-56.
- [47] K. Mathis, K. Horvath, G. Farkas, H. Choe, K.S. Shin, A. Vinogradov, Investigation of the Microstructure Evolution and Deformation Mechanisms of a

- Mg-Zn-Zr-RE Twin-Roll-Cast Magnesium Sheet by In-Situ Experimental Techniques, *Materials* 11(2) (2018).
- [48] J. Sun, L. Jin, J. Dong, W.J. Ding, A.A. Luo, Microscopic deformation compatibility during monotonic loading in a Mg-Gd-Y alloy, *Materials Characterization* 119 (2016) 195-199.
- [49] D. Raabe, M. Sachtleber, Z. Zhao, F. Roters, S. Zaeferrer, Micromechanical and macromechanical effects in grain scale polycrystal plasticity experimentation and simulation, *Acta Materialia* 49(17) (2001) 3433-3441.
- [50] F. Delaire, J.L. Raphanel, C. Rey, Plastic heterogeneities of a copper multicrystal deformed in uniaxial tension: Experimental study and finite element simulations, *Acta Materialia* 48(5) (2000) 1075-1087.
- [51] D.B. Xia, G.S. Huang, Q.Y. Deng, B. Jiang, S.S. Liu, F.S. Pan, Influence of stress state on microstructure evolution of AZ31 Mg alloy rolled sheet during deformation at room temperature, *Mat Sci Eng a-Struct* 715 (2018) 379-388.
- [52] M.R. Barnett, Z. Keshavarz, M.D. Nave, Microstructural features of rolled Mg-M-1Zn, *Metall Mater Trans A* 36a(7) (2005) 1697-1704.
- [53] Y.B. Chun, C.H.J. Davies, Texture effects on development of shear bands in rolled AZ31 alloy, *Mat Sci Eng a-Struct* 556 (2012) 253-259.
- [54] F. Kabirian, A.S. Khan, T. Gnäupel-Herlod, Visco-plastic modeling of mechanical responses and texture evolution in extruded AZ31 magnesium alloy for various loading conditions, *International Journal of Plasticity* 68 (2015) 1-20.
- [55] R. Pippan, S. Wurster, D. Kiener, Fracture mechanics of micro samples: Fundamental considerations, *Mater Design* 159 (2018) 252-267.
- [56] Z.R. Zeng, M.Z. Bian, S.W. Xu, C.H.J. Davies, N. Birbilis, J.F. Nie, Effects of dilute additions of Zn and Ca on ductility of magnesium alloy sheet, *Mat Sci Eng a-Struct* 674 (2016) 459-471.
- [57] T. Obara, H. Yoshinga, S. Morozumi,  $[11\bar{2}2]$  Slip System in Magnesium, *Acta Metall Mater* 21(7) (1973) 845-853.
- [58] J. Koike, R. Ohyama, Geometrical criterion for the activation of prismatic slip in AZ61 Mg alloy sheets deformed at room temperature, *Acta Materialia* 53(7) (2005) 1963-1972.
- [59] Z. Keshavarz, M.R. Barnett, In-situ investigation of twinning behaviour in Mg-3Al-1Zn, *Magnesium Technology 2005* (2005) 171-175.
- [60] M.R. Barnett, M.D. Nave, A. Ghaderi, Yield point elongation due to twinning in a magnesium alloy, *Acta Materialia* 60(4) (2012) 1433-1443.
- [61] K. Hagihara, T. Mayama, M. Honnami, M. Yamasaki, H. Izuno, T. Okamoto, T. Ohashi, T. Nakano, Y. Kawamura, Orientation dependence of the deformation kink band formation behavior in Zn single crystal, *International Journal of Plasticity* 77 (2016) 174-191.
- [62] H.Y. Gao, K. Ikeda, T. Morikawa, K. Higashida, H. Nakashima, Analysis of kink boundaries in deformed synchronized long-period stacking ordered magnesium alloys, *Mater Lett* 146 (2015) 30-33.
- [63] B.L. Xi, G. Fang, S.W. Xu, Multiscale mechanical behavior and microstructure evolution of extruded magnesium alloy sheets: Experimental and crystal plasticity

analysis, Mater Charact 135 (2018) 115-123.

[64] L.Y. Zhao, Y.C. Xin, Y. Wu, Q. Liu, The texture dependence of strength in slip and twinning predominant deformations of Mg-3Al-1Zn alloy, Mat Sci Eng a-Struct 717 (2018) 34-40.

[65] D.D. Yin, Q.D. Wang, C.J. Boehlert, Z. Chen, H.M. Li, R.K. Mishra, A. Chakkedath, In-Situ Study of the Tensile Deformation and Fracture Modes in Peak-Aged Cast Mg-11Y-5Gd-2Zn-0.5Zr (Weight Percent), Metallurgical and Materials Transactions A 47(12) (2016) 6438-6452.

[66] D. Steglich, Y. Jeong, M.O. Andar, T. Kuwabara, Biaxial deformation behaviour of AZ31 magnesium alloy: Crystal-plasticity-based prediction and experimental validation, Int J Solids Struct 49(25) (2012) 3551-3561.

[67] J.Y. Min, T.B. Stoughton, J.E. Carsley, B.E. Carlson, J.P. Lin, X.L. Gao, Accurate characterization of biaxial stress-strain response of sheet metal from bulge testing, International Journal of Plasticity 94 (2017) 192-213.

# Microscopic deformation compatibility during biaxial tension in AZ31 Mg alloy rolled sheet at room temperature

Dabiao Xia<sup>a,b</sup>, Guangsheng Huang<sup>a,b,c,\*</sup>, Shuaishuai Liu<sup>a,b</sup>, Aitao Tang<sup>a,b,c</sup>, Serge Gavras<sup>d</sup>, Yuanding Huang<sup>d</sup>, Norbert Hort<sup>d</sup>, Bin Jiang<sup>a,b,c\*</sup>, Fusheng Pan<sup>a,b,c</sup>

<sup>a</sup> State Key Laboratory of Mechanical Transmission, College of Materials Science and Engineering, Chongqing University, Chongqing 400044, China

<sup>b</sup> National Engineering Research Center for Magnesium Alloys, Chongqing University, Chongqing 400044, China

<sup>c</sup> Chongqing Research Center for Advanced Materials, Chongqing Academy of Science & Technology, Chongqing 401123, China

<sup>d</sup> MagIC-Magnesium Innovation Centre, Helmholtz-Zentrum Geesthacht, Max-Planck-Str. 1, 21502 Geesthacht, Germany

## Abstract

In this paper, *in situ* electron back scattered diffraction combined with scanning electron microscopy and digital image processing techniques were used to study the microscopic deformation compatibility of AZ31 Mg alloy rolled sheets with strong basal texture during biaxial tension at room temperature. **The results firstly quantitatively showed that the distribution of microscopic strain in AZ31 rolled sheet was inhomogeneous during formation.** Strain concentrations happened in some regions even at early stage of deformation. Short distorted bands also appeared in these regions and extended to connect each other with increasing macroscopic strain. The appearance of distorted bands play an important role in strain compatibility since the materials lack easy deformation modes at room temperature. Besides slips and twins, the grain distortion should also be an indispensable mechanism in accommodating plastic deformation in some parts in distorted bands. **According to the**

---

\* Corresponding author: College of Materials Science and Engineering, Chongqing University, Chongqing 400044, China.

E-mail address: gshuang@cqu.edu.cn (G.S. Huang), binjiang@cqu.edu.cn (B. Jiang).

analysis from the Schmid factor, the geometric compatibility factors and slip trace identification, the comprehensive effect of strong basal texture and biaxial tensile stress state not only led to the quite low SFs for prismatic <a>, pyramidal <a> slips and tensile twinning, but limited the compatibility between slip systems and tensile twins. This mechanism was the main reason for the lack of easy deformation modes and the appearance of distorted bands, which further led to the inhomogeneous strain distribution at room temperature. Therefore, the formability of Mg alloys rolled sheets with strong basal texture was weakened at room temperature.

*Key words:* magnesium alloy; deformation compatibility; microstructure; in situ EBSD; basal texture

## **1. Introduction**

In recent years, the applications of magnesium alloys have increased rapidly for automotive, aerospace and communications industries for which weight reduction is highly required [1-4]. The Mg alloy rolled sheets even draw special attention due to their great potential in future applications [5-7]. However, the adoption of Mg alloy rolled sheets remains limited compared with that of steel and aluminum alloys [8-10]. Their poor deformability at room temperature mainly results from their intrinsic hexagonal close packed crystal structure [11-14]. Hence, continuous efforts have been made to improve the formability of Mg alloy rolled sheets and to extend their commercial applications in recent years.

The fundamental challenge to improve the formability of Mg alloy rolled sheet is to activate more deformation modes and improve the compatibilities to coordinate the macroscopic plastic flow. The specific methods include grain coarsening, basal texture randomizing/weakening, alloying and raising the forming temperature, etc. The coarse grains in Mg alloys can significantly enhance the twin formation. The lattice rotation caused by twinning behavior induces the strain in the thickness direction by enhancing the slip activities [15, 16]. In addition, non-basal slip systems will dominate the material flow instead of basal slip with increasing grain size. The compatibilities between different deformation modes are promoted as well [17, 18].

All these improvements can benefit the formability of Mg alloy rolled sheets.

The initial texture can also influence the sheet formability significantly. With specific texture orientation and distribution, the critical resolved shear stress (CRSS) of prismatic slip and twinning are decreased [19, 20]. Similar effects were also achieved by randomizing or weakening the basal texture [21-25]. An effective approach to randomize/ weaken the texture is the utilization of rare earth (RE) elements such as Gd, La, Nd, Ce and Y [12, 26-29]. With RE addition,  $CRSS_{prism}/CRSS_{twinning}$  and  $CRSS_{pyr}/CRSS_{twinning}$  ratios decrease which can improve the **activation** of prismatic and other non-basal slip systems [30-33]. The results based on visco-plastic self-consistent (VPSC) simulation indicated that the formability of Mg alloys can be efficiently improved with increasing activities of prismatic slips and non-basal slips [34-36]. However, they were **mostly obtained** based on the theoretical simulations. The actual **activation** ratios between different deformation modes are still unclear since the practical statistics are difficult to **obtain**. Moreover, although the accommodation between slips and twins should be important in coordinating plastic strain during formation, the practical observations about the accommodating behaviors on microscopic **scales** were rarely reported. The slow development of biaxial tension testers is likely to be the main reason for the previous lack of information [37, 38].

*In situ* experimental methods and digital image processing techniques have been well developed **in recent years**. These techniques can provide a new insight into the **evolution** of microstructure and microscopic strain distribution in Mg alloys during deformation [20, 39-45]. **The *in situ* acoustic emission techniques have been widely used to study the local dislocation activity** [46, 47]. With *in situ* SEM experiments, the relative contributions of different slip systems in **the Mg alloy AZ31** during uniaxial tensile were proved to be: 41% basal, 44% prismatic  $\langle a \rangle$  and 15% pyramidal  $\langle a+c \rangle$  at 423 K [39]. The *in situ* electron back scattered diffraction (EBSD) results indicated that tensile twin chains **were a type of** strain compatibility behaviors among twin variants in adjacent grains, rather than twins **moving** across grain boundaries in

adjacent grains [40]. This effect, in combination with digital image correlation, proved that microscopic strain distribution was significant inhomogeneous in copper, aluminum and Mg alloys during uniaxial tension [48-50]. However, reports about microstructural evolutions for Mg alloys during formation were quite few, especially for the relationship between strain localizations and activities of dislocations obtained from *in situ* experiments [51, 52].

AZ31 rolled sheets were widely used materials, which is often deformed under biaxial tensile stress state (BTSS) during stamping, bending or other complicated forming processes. In the present work, biaxial tension tests for the hot-rolled AZ31 sheets were conducted using a new specific device to study their microstructural evolutions during forming. The new device is simple, cheap and functional for micro biaxial tension tests. The combination of *in situ* EBSD, scanning electron microscopy (SEM) and image processing techniques were firstly used to characterize the microstructural changes as well as the quantitative measurement of microscopic strain distribution in AZ31 rolled sheets during formation.

## 2. Material and methods

The material in this investigation was a commercial AZ31 Mg alloy hot rolled sheet from Yinguang Magnesium Industry Group Co., LTD. The sheet was then fully recrystallized at 450 °C for 20 min. The high annealing temperature is beneficial for grains to grow up and consequently the formability could be improved as well [15]. In order to investigate the anisotropy of the annealed samples in rolling direction (RD)-transverse direction (TD) plane, the typical tensile tests were conducted using the specimens with a gauge length of 12.5 mm, width of 6 mm and thickness of 0.6 mm. The strain rate was set as  $10^{-3} \text{ s}^{-1}$ .

The samples for biaxial tension testing were prepared by sectioning to the dimensions shown in Fig. 1a and mechanically ground on the RD-TD plane of the sheet. The ground samples were electro-polished using the commercial electrolyte AC II at 0 °C, with a voltage of 20 V for 120 s. The freshly polished sample was set

into the **biaxial tension device** shown in Fig. 1(b). This device is similar to the **equipment** used for Erichsen tests except that the sample was held by tightening the nut and the punch was driven by rotating the loading screw (Fig. 1b). The dome height of the sample was equal to the stroke of the punch. According to five pre-tests, the average dome height before fracture was about 1.50 mm. Hence, in the present *in situ* tests, the interrupting punch strokes were selected with 0.12 mm, 0.24 mm, 0.36 mm, 0.48 mm, 0.72 mm, 0.84 mm, 1.08 mm and 1.50 mm (broken).

**Automatic *in situ* EBSD measurements were performed using a JEOL JSM 7800F field emission SEM equipped with a HKL Channel 5.0 software using a step size of 0.6  $\mu\text{m}$ . Before deformation, the microstructure of the initial sample's center was measured by EBSD once. In order to calculate the following microscopic strain, micro grids, having a step size of 10  $\mu\text{m}$  and a width of 200  $\mu\text{m}$  [48], were deposited on the EBSD-measured region of the sample using a Zeiss AURIGA SEM-Focused ion beam miller (FIB). After the FIB process, the surface morphology (including the grids) of the sample was captured and saved as high-resolution images using SEM. Then, the whole device was taken out from SEM. The first deformation step was proceeded by rotating the screw to the corresponding degree so that the dome height would be 0.12 mm. The average speed of the punch was about 0.36 mm/min. After deformation, the device was set back into the SEM. The morphology of the deformed sample was **imaged** again and the EBSD measurement was conducted as well. The subsequent similar steps were carried out in the same way until the fracture of the sample occurred (with 1.50 mm dome height) [51].**

**The digital image process program was then developed to convert the collected high-resolution images to grayscale, then, count the total pixels in each grid. The total number change of pixels in the grid was treated as the area change of the grid with different dome height. The corresponding microscopic strain  $\varepsilon$  of one grid was calculated using Eq. (1):**

$$\varepsilon = \frac{S_i - S_0}{S_0} \quad \text{Eq. (1)}$$

$S_0$  is the initial area of the grid and  $S_i$  is the corresponding area after deformation. **This program also gave the gravity center of the grid to assign it the total**

microscopic strain in the grid.

### 3. Results

#### 3.1. Initial microstructure and mechanical properties

An EBSD map of the alloy in the initial condition and corresponding texture pole figure are shown in Fig. 2a and b respectively. The rolled sheet exhibits a fully recrystallization microstructure with an average linear intercept grain size of  $\sim 30 \mu\text{m}$ . Some large grains have a size of  $\sim 80 \mu\text{m}$  while some other grains can be as small as  $\sim 15 \mu\text{m}$ . Their influences on plastic deformation may be different. Fig. 2b reveals a strong  $\{0001\}$  basal texture of the sheet. The typical uniaxial tensile true stress-strain curves of the annealed samples are shown in Fig. 2c. It indicates that the curves in three directions are quite close. Hence, the sheet is regarded as isotropic in RD-TD plane in this paper.

#### 3.2 Quantitative investigations on microscopic strain evolution

Fig. 3a ~ h show the microstructural evolution during the biaxial tension superimposed with strain maps. The lines of the grids were marked again to make them clear in Fig. 3 and other subsequent figures. In Fig. 3, the strain maps exhibit inhomogeneous strain distribution. The range of the strain is approximately  $-0.4 \sim 1.2$ . Tensile and compressive strains coexist. The high-level microscopic strains appeared in certain regions even with relatively low dome height of 0.12 mm (Fig. 3a). Their locations were quite stable during formation and hardly changed. With increasing dome height, the strain values in high-strain regions also increase.

The quantitative calculations of the inhomogeneous strain distribution at different strain levels are shown in Fig. 4. Fig. 4a exhibits the normalized strain distribution measured from Fig. 3 at different strain levels. The distribution of local normalized strain is in a range of  $(-1 \sim 7)$ . The fraction of the normalized strain with  $\sim 1$  increases with increasing macroscopic strain. However, the fraction  $\sim 3$  is still notable during the whole formation. This means that the strain concentration always exists. The strain standard deviation at different scale lengths is shown in Fig. 4b. Its

definition was described by Sun et al. [48]. It decreases with the increment of scale length at every strain level. This suggests that the inhomogeneous strain distribution is not in macro-scale (such as shear bands), but rather than at the grain level, similar to that under uniaxial tensile stress state (UTSS) [48].

The morphological evolution of the meshed region is shown in Fig. 5. Slip traces and shear stages began to appear early with 0.12 mm dome height (Fig. 5b1 and b2). Secondary twins are shown to exist in the sheared stages using orientation identification method (Fig. 5b2 and 5b3). The appearance of secondary twins can be attributed to their large matrix grain, which typically causes a stress concentration at grain boundaries. In addition, the short distorted bands (DBs) are observed in some regions as well (Fig. 5b). Due to the fact EBSD measurements are not functional in these bands, the determination that twins are in them or not is not known. With the dome heights increasing to 1.50 mm (broken), the DBs extend to connect each other (Fig. 5c). The concentration of secondary twins has given rise to the occurrence of a micro crack. This crack is numbered as crack-1, as depicted in Fig. 5c. Fig. 5d presents that shear bands exist in RD-normal direction (ND) plane after fracture. The angle between RD-TD plane and shear bands is  $\pm \sim 30^\circ$ , which is typical for AZ31 rolled sheet with a strong basal texture [53].

## 4. Discussion

### 4.1. Evolution of microscopic strain distribution

Since the microscopic strain is inhomogeneous, the strain rate in different regions should be inhomogeneous as well. It was reported that both the activation of deformation modes and the strain hardening effect in Mg alloys are sensitive to the strain rate [54]. In the present work, the speed of the punch is an estimated average value. The strain rate at the center of the sample is not linearly related with the speed of punch. Hence, the distribution of the strain evolution standard deviation ( $S_{SE}$ ) instead of the true strain rate is calculated for each grid in the meshed region during the biaxial tension. The definition of  $S_{SE}$  is introduced as Eq. (2):

$$S_{SE} = \sqrt{\frac{1}{N} \sum_{i=1}^N (\varepsilon_e - \bar{\varepsilon}_e)^2}$$

Eq. (2)

$\varepsilon_e$  is one measured strain value of one grid,  $\bar{\varepsilon}_e$  the average strain of this grid during the whole deformation and  $N$  is the total number of the measured strain values.

As an index of one grid's strain fluctuation,  $S_{SE}$  can qualitatively represent the average strain rate of the grid. The calculation results (Fig. 6a) suggest that not only these regions with intermediate-level strains but also some grids with **intermediate**-level strains have a high  $S_{SE}$ . Normally, DBs and micro cracks prefer to form in those grids with high  $S_{SE}$ , rather than with high-level strains (Fig. 6b). It can then be concluded that the appearance of DBs should contribute to the high strain rate, instead of high-level strain. The fracture may occur along these DBs owing to the stronger strain strengthening caused by the high strain rate if the friction between the punch and the sample is zero.

Fig. 6a also indicates that the highest  $S_{SE}$  appears near crack-1, not in DBs. After numbering all the grids in Fig. 6a, the microscopic strain evolutions of some grids with high  $S_{SE}$  near crack-1 are shown in Fig. 6c and those in DBs are shown in Fig. 6d. Most grids in Fig. 6c have a fluctuating strain evolution while the strains of most grids in Fig. 6d increase monotonically. The highest  $S_{SE}$  should be caused by the fluctuating strain. Since the secondary twins are continuously concentrated near the crack-1, it can be easily inferred that the shear strain caused by secondary twins should be the main reason for the fluctuating strain in Fig. 6c. That is to say, the high strain rate caused by secondary twin should be an important mechanism responsible for the fracture in Mg alloys [55]. **In general, a possible way to prevent Mg alloy rolled sheets from prematurely fracturing is by inhibiting the high-level strain rate caused by the inhomogeneity of strain distribution.**

#### 4.2. Relationship between SF and microscopic strain

From Fig. 3 and Fig. 6, it can be found that most regions with high-level strain or high strain rate are distributed in DBs. It can thus be inferred that the appearance of DBs is an important mode for strain accommodation. As it is well known, in sheets

for one deformation mode with large value of SF, a lower applied stress is required to activate its operation and its deformation becomes easier to be coordinated as well [56]. Firstly, the relationship between DBs and SFs of five important modes in Mg alloys were investigated. The calculation method for SF under different stress states was introduced from Xia *et al.* [51]. The results are shown in Fig. 7. It indicates that the SFs for prismatic  $\langle a \rangle$  and tensile twinning are quite low. The SF for basal  $\langle a \rangle$  is **also not much higher**. Even though the SF for pyramidal  $\langle a+c \rangle$  is high, its contribution to deformation should be ignored due to the very high critical resolved shear stresses (CRSS) [13, 57, 58]. Compared with Fig. 6b and Fig. 7, however, it seems that there is no clear relationship between SFs and DBs. **This** infers that the appearance of DBs and their gradually joining together with increasing dome height may not be or may not only be dominated by SF.

It is notable that most of the SFs under BTSS are quite low, especially for prismatic  $\langle a \rangle$  and tensile twinning. The SFs for the same five deformation modes under UTSS were calculated as a comparison (Fig. 8). The loading direction is along RD. The SFs for prismatic  $\langle a \rangle$ , pyramidal  $\langle a \rangle$  and tensile twinning under UTSS are much higher than those under BTSS. The activation for these three modes are much harder under BTSS. Mg alloys are well known for having a lack of easy deformation modes at room temperature, even under uniaxial stress state. In the present investigation, the lack of deformation modes should be more serious. The inhomogeneous strain distribution should also be partly influenced by such “*hardening*” caused by low SFs.

#### 4.3. Deformation compatibility in DBs

The strain compatibility offered by DBs should depend on the local strain compatibility in themselves. To study the local strain compatibility in DBs, the compatibility factors ( $m'$ ) was employed [59, 60]. The microstructures and morphological evolutions of three different representative regions in DBs are presented in Fig. 9-11. Since just basal  $\langle a \rangle$  and prismatic  $\langle a \rangle$  slip traces were observed, all their possible orientations for the studied grains are listed in Fig. 9-11 as

well [17]. The corresponding SFs and  $m'$  values for the investigated grains in Fig. 9-11 are listed in Tab. 1-3.

In Fig. 9, a total of seven grains are present in the region covered by the micrograph. Only basal  $\langle a \rangle$  slip traces were observed in **both grains** A and D with 0.12 mm dome height. No twins were identified by EBSD. Tab. 1 suggests that the corresponding SFs and  $m'$  values for these two grains are relatively higher than others. With the dome height increasing to 0.84 mm, the short prismatic  $\langle a \rangle$  slip traces appear **in grain** E. However, both the corresponding SF and  $m'$  values for the prismatic  $\langle a \rangle$  in grain E are relatively low (Tab. 1). It can be inferred that the activation of prismatic  $\langle a \rangle$  **in grain** E should be related to the **high-level** local stress. More importantly, “grain distortions” appear **in grains** B, E and F, which are free of slip traces during the whole tension (Fig. 9). The high-level strains are also concentrated in those grids with grain distortions. The morphology of the folds **in grain** F are similar to kink bands reported in the previous papers [61, 62]. In kink bands, non-basal slip is the dominant deformation mode. Since EBSD measurement was not available in these DBs, the stress concentration should be high. In these “grain distortions”, non-basal slip, contraction twins or secondary twins should be involved. All these phenomena suggest that the deformation compatibility in these regions is poor.

As a comparison, in Fig. 10, the basal traces appear **in grains** H, J and K with 0.12 mm dome height. Their corresponding SFs and  $m'$  values are much higher than the other five grains (Tab. 2). In addition, the short prismatic traces are observed **in grains** L and M. The SFs for their prismatic  $\langle a \rangle$  are low but their  $m'$  values are high. Tensile twins are found in grain N as well. With the dome height increasing to 0.84 mm (0.138 macroscopic strain), several shear ledges are found **in grain** J. The micro strains are higher in these grids crossed by the shear ledges. According to the identification in Fig. 5b2 and b3, it can be concluded that the secondary twins should also exist in these shear ledges (Fig. 10). The stress level here is higher than other parts. However, the SFs and  $m'$  values in Tab. 2 are higher than those in Tab. 1. No

grain distortion is found in this region and the strain distribution is a little more homogeneous as well. All these phenomena suggest that the deformation compatibility here is better than that in Fig. 10.

In Fig. 11, approximately seven of the eight grains are full of slip traces with 0.12 mm dome height. Most of matrix in grain P is occupied with tensile twins. Basal traces are found in the tensile twins. The corresponding SFs or  $m'$  values in Tab. 3 are higher than those in Tab. 2 and much higher than those in Tab. 1. It should be noted that the  $m'$  between tensile twin and basal slip is theoretically maximum at 0.46 in grain F in Tab. 3. Besides, the SF of tensile twin in grain P is the SF for the activated variant, so is the  $m'$ . With the dome height increasing to 0.84 mm, the basal traces can be observed in every grain, especially for the tensile twins. Since the strain of most grains is high, the micro cracks appear at grain boundaries. A grain distortion is observed at the boundary **between grains** J and Q as well. There should be no secondary twins since no shear ledges are observed in Fig. 11. The stress level may be lower than that in Fig. 10 or Fig. 9. Hence, the deformation accommodation in Fig. 11 should be the best among these three regions.

For slip-dominated deformation, strain localization at the *inter-granular* scale is located at the place where both  $m'$  values and high SFs for certain deformation modes in adjacent grains should be met under uniaxial stress state [63]. A low  $m'$  value usually leads to a high boundary obstacle effect [64]. However, no matter how good the compatibility is in these regions, DBs (or **high-level** strains) still concentrate in these regions and offer important strain compatibility for deformation. The distribution of DBs or inhomogeneous strains should not result from good or poor deformation compatibility in grains.

#### 4.4. Influences of stress state and texture on microscopic strain distribution

A strong basal texture can lead to a lack of easy deformation modes in Mg alloys at room temperature. Chun *et al.* [53] reported that with a strong basal texture, more pronounced shear bands appeared in Mg alloys during rolling due to the lack of deformation modes. The formability of Mg alloy rolled sheets also decreased with a

stronger basal texture at room temperature. The mechanism is that a limited amount of prismatic  $\langle a \rangle$  slip was activated in a strong basal texture, further leading to an increase of shear bands [20]. In the present investigation, strong basal texture also exists (Fig. 2b) and shear bands **are observed** (Fig. 5d). Most of the observed traces are identified as the basal slip as shown in Tab. 4 in which the total number of grains in meshed regions are 244 and traces of other kinds of slip models are not found. The grains with the **presence** of prismatic slip increases slowly from 2 to 8 with dome height increasing from 0.12 mm to 0.84 mm. The prismatic slip traces are much less than basal traces during the **entire** deformation. Non-basal slip traces are rarely observed. Yin *et al.* [65] listed all three reasons for the absence of slip traces: (1) the amount of mobile dislocations was not large enough to form an obvious slip trace, (2) the Burgers vector of the dislocation was parallel to the sample surface, and (3) the dislocation did not move to the sample surface. In the present work, the main reasons for very few prismatic  $\langle a \rangle$  or non-basal slip traces should be reason (1). Hence, basal slip should always be the main deformation **mode, which** offers the most deformation accommodation during deformation under BTSS. There is a lack of easy deformation modes in AZ31 rolled sheets during forming at room temperature. In this case, the stress rapidly concentrates in some regions, which finally causes grain distortion or DBs. This phenomenon should belong to a kind of inhomogeneous geometric texture softening [53].

With the same strong texture, the SFs in Fig. 8 under UTSS are much higher than those in Fig. 7 under BTSS. The deformability for Mg alloys under UTSS is better than that under BTSS [51]. The strong basal texture is not the only reason for the lack of easy deformation modes or for the inhomogeneous strain distribution. The previous works [51] have proved that the BTSS dominated the distribution of SF on (0001) pole figure. The SFs for prismatic  $\langle a \rangle$ , pyramidal  $\langle a \rangle$  and tensile twinning rapidly reduces when two conditions are simultaneously satisfied: (i) Mg alloy sheet is under BTSS in plane; (ii) the intensity of the basal texture is high (both satisfied in this paper). In addition, the accommodations between tensile twins and prismatic  $\langle a \rangle$ ,

pyramidal  $\langle a \rangle$  and tensile twinning are also deteriorated because of BTSS. More importantly; the BTSS can even lead to a higher tangent modulus, which is significant higher than that under UTSS. The strain hardening in Mg alloys is different under BTSS as well [66, 67]. The deformation stress is much higher under BTSS than that under UTSS. This may lead to the increase of stress or strain concentration level. Hence, the BTSS should also be an important reason responsible for the inhomogeneous strain distribution. Therefore, if it is not possible to weaken the strong basal texture, the BTSS should be adjusted to obtain a better formability of Mg alloy rolled sheets. A method to adjust the stress state during formation of Mg alloy rolled sheets is currently being investigated.

## 5. Conclusion

In this paper, *in situ* biaxial tension in SEM combined with EBSD and a digital image processing techniques were applied to quantitatively investigate the forming behavior of Mg alloy rolled sheets with strong basal texture at room temperature.

The following conclusions were made:

- (1) The distribution of microscopic strain in AZ31 rolled sheet is quite inhomogeneous during forming at room temperature. The micro strain distribution under BTSS is more inhomogeneous than that under UTSS. This inhomogeneity of strain is not in the macro-scale, but at grain level. The deformability is limited by the inhomogeneity of strain distribution.
- (2) The formation of DBs is an important mode for strain compatibility. The compatibility between different deformation modes in DBs could be good, poor or intermediary. It is primarily due to the corresponding SFs for the activated modes in the adjacent grains. However, the strain rate in DBs is always higher than other regions.
- (3) In the regions with poor compatibility, the activation of the easiest modes (basal  $\langle a \rangle$ , prismatic  $\langle a \rangle$  and tensile twinning) are limited. In this case, the “grain distortion” resulted from the high-level stress concentration, which plays an

important role in accommodating deformation. However, the grain distortions are often accompanied by micro cracks, which may lead to fracture. Hence, creating grain distortions should be avoided in order to improve the formability of Mg alloy sheets.

- (4) By limiting the SFs for deformation modes and the compatibility between slips and twinning, both the strong basal texture and the BTSS are the main reasons for the lack of easy deformation modes. They further cause the formation of DBs or inhomogeneous strain distribution in AZ31 rolled sheet. Hence, Mg alloy sheets with strong basal texture deform under BTSS during formation should be avoided.

### **Acknowledgements**

This work was supported by The National Key Research and Development Plan (2017YFB1300700), The National Natural Science Foundation of China (No. 51671041, NO. 51531002 and NO. U1764253) and Natural Science Foundation of Chongqing (cstc2017jcyjBX0040). The China Scholarship Council is also gratefully acknowledged for financial support for Dabiao Xia (201806050045).

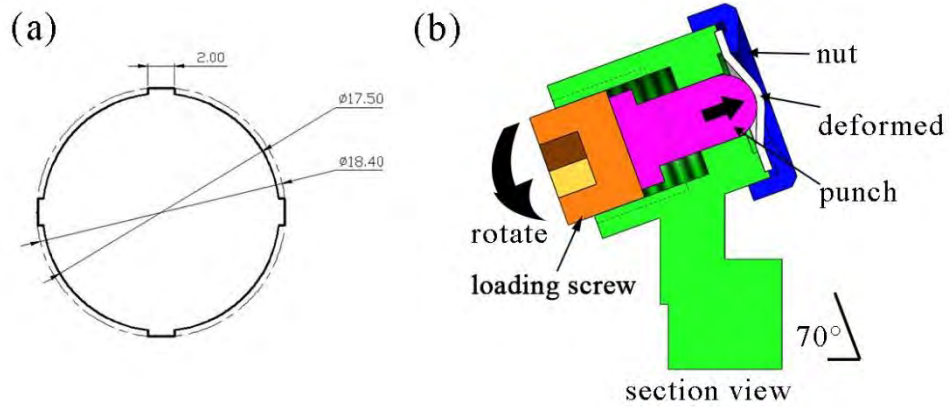


Fig. 1. (a) Dimensions of samples for biaxial tension and (b) schematic of micro biaxial tension system for in-situ EBSD.

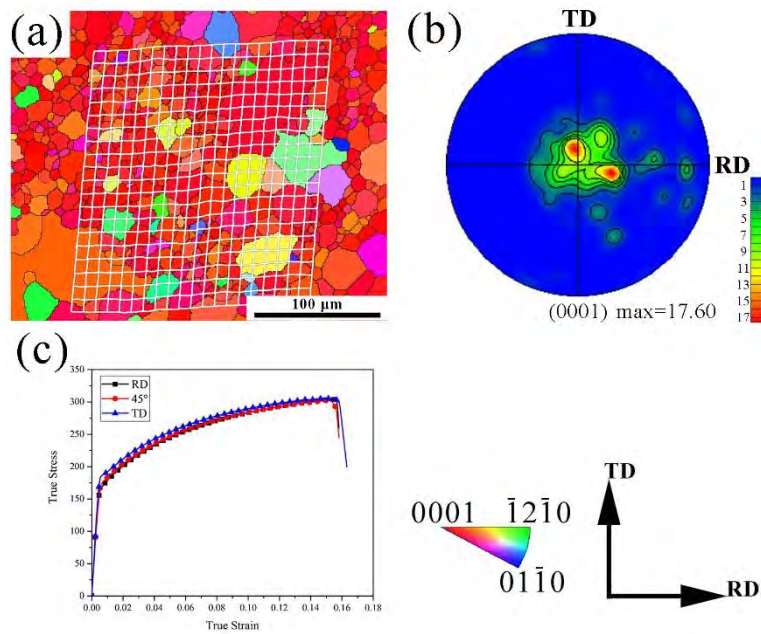


Fig. 2. (a) Initial microstructure, (b) (0001) pole figure and (c) typical uniaxial tensile true stress-strain curves for the annealed AZ31 alloy sheet along RD, TD and 45 °. The grids in (a) were superimposed to show their position.

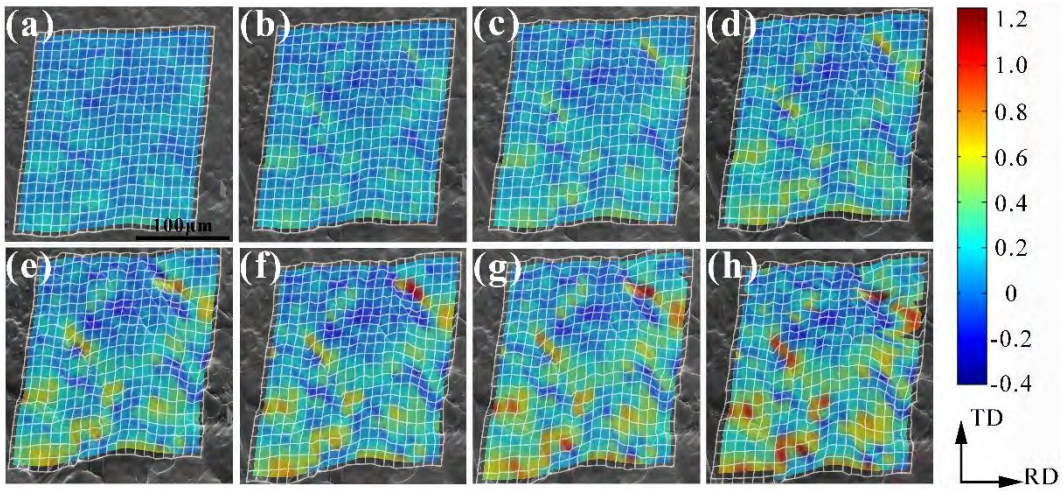


Fig. 3. Strain evolution maps (a) 0.12, (b) 0.24, (c) 0.36, (d) 0.48, (e) 0.72, (f) 0.84, (g) 1.08 and (h) 1.50 mm dome height.

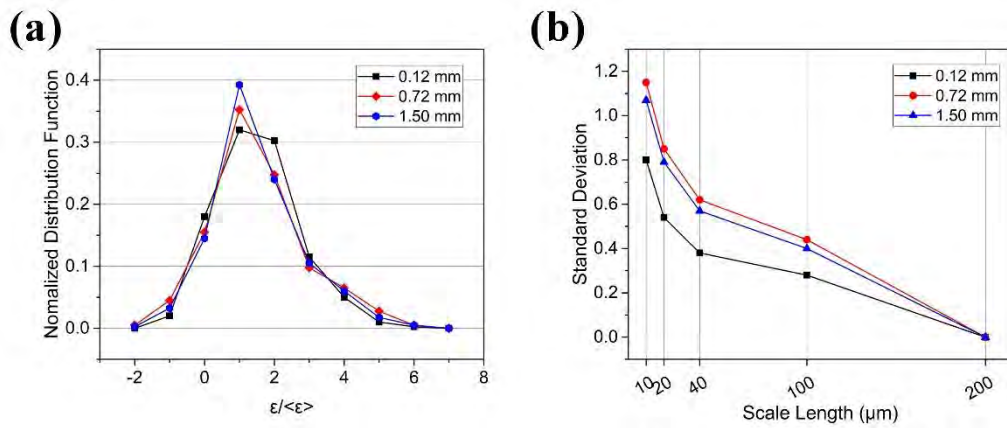


Fig. 4. (a) Normalized strain distribution and (b) standard deviation of strain as a function of scale length at different strain levels ( $\epsilon$  is the measured strain of every grid and  $\langle \epsilon \rangle$  is the average strain of the **entire** meshed region).

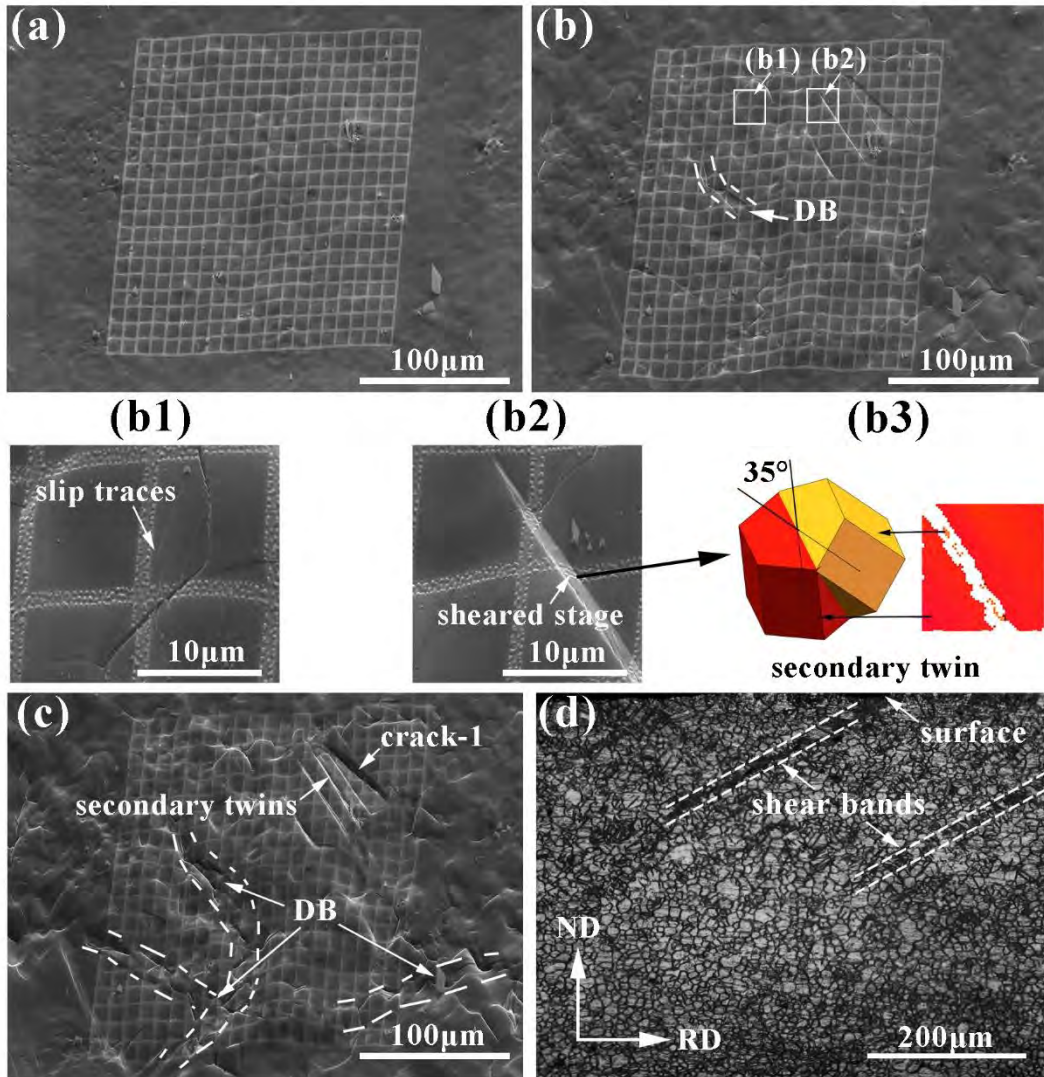


Fig. 5. Morphological evolution with (a) 0 mm, (b) 0.12 mm, (c) 1.50 mm and (d) the microstructure in RD-ND plane with 1.50 mm dome height. At the top of (d) is the measured surface of the sample.

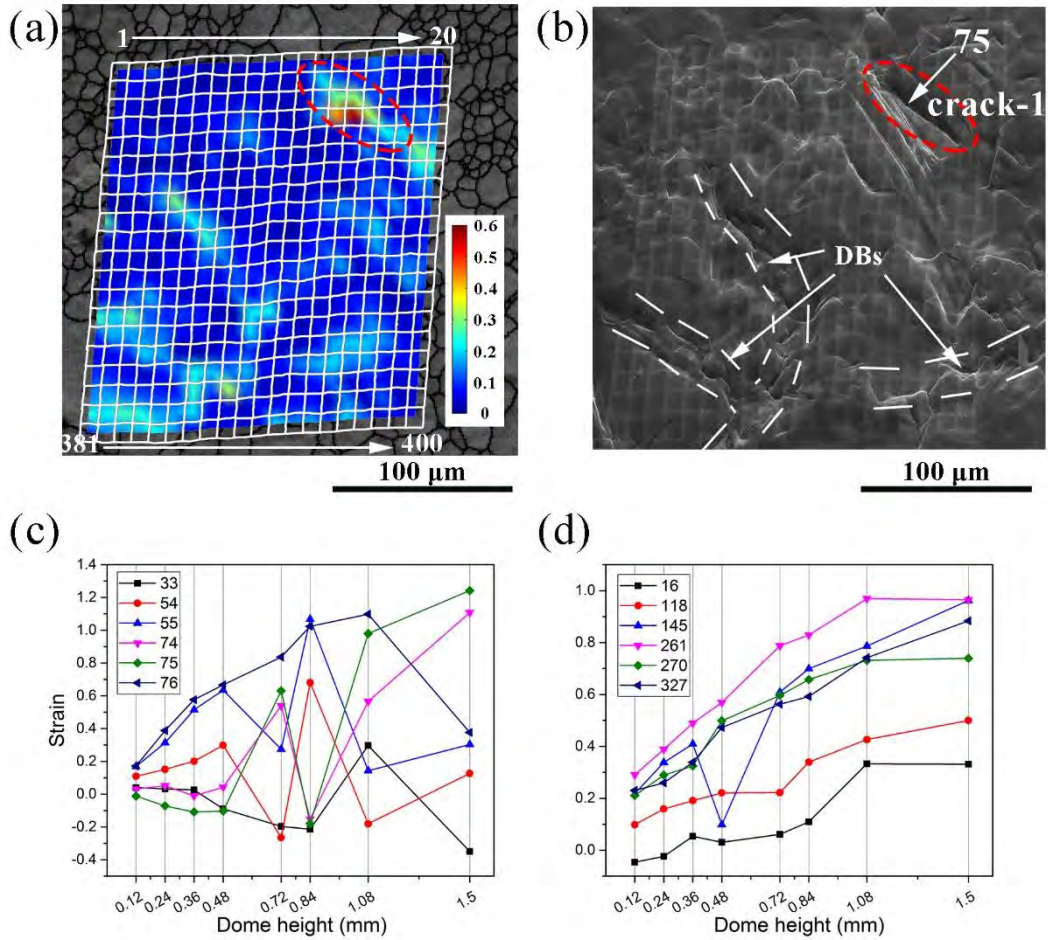


Fig. 6. (a) Distribution of  $S_{SE}$  with gird numbers, (b) the shear bands and microscopic cracks appeared when the dome height was 1.08 mm, “75” is the gird number, (c) the fluctuant strain of some grids and (d) the monotonic increasing strain of some grids.

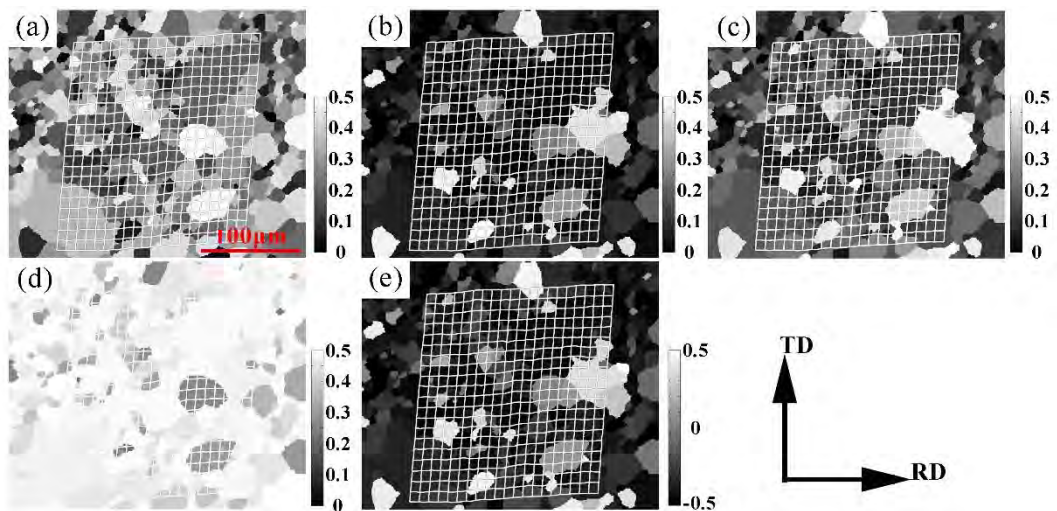


Fig. 7. Distribution of SF for (a) basal  $\langle a \rangle$ , (b) prismatic  $\langle a \rangle$ , (c) pyramidal  $\langle a \rangle$ , (d) pyramidal  $\langle a+c \rangle$  and (e) tensile twinning under BTSS.

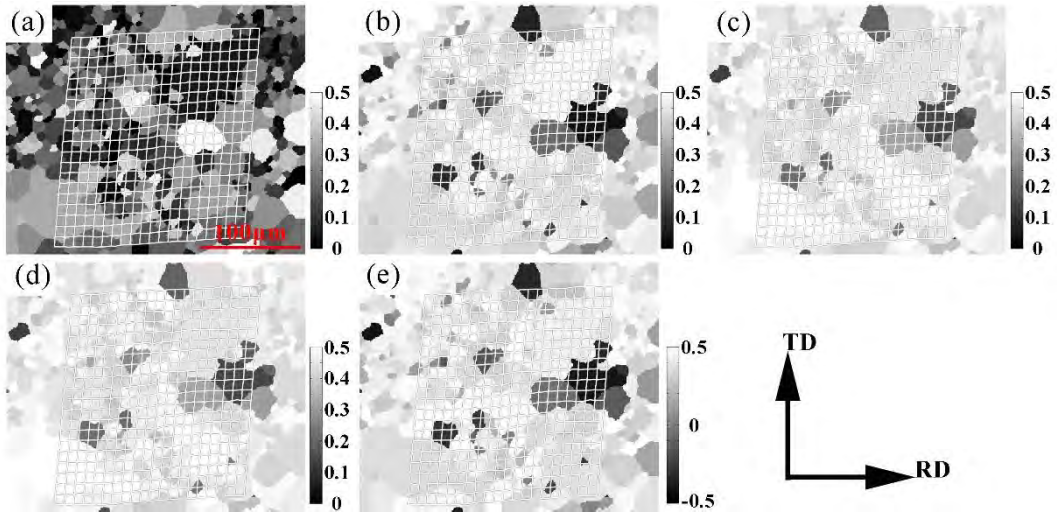


Fig. 8. Distribution of SF for (a) basal  $\langle a \rangle$ , (b) prismatic  $\langle a \rangle$ , (c) pyramidal  $\langle a \rangle$ , (d) pyramidal  $\langle a+c \rangle$  and (e) tensile twinning under UTSS with loading along RD.

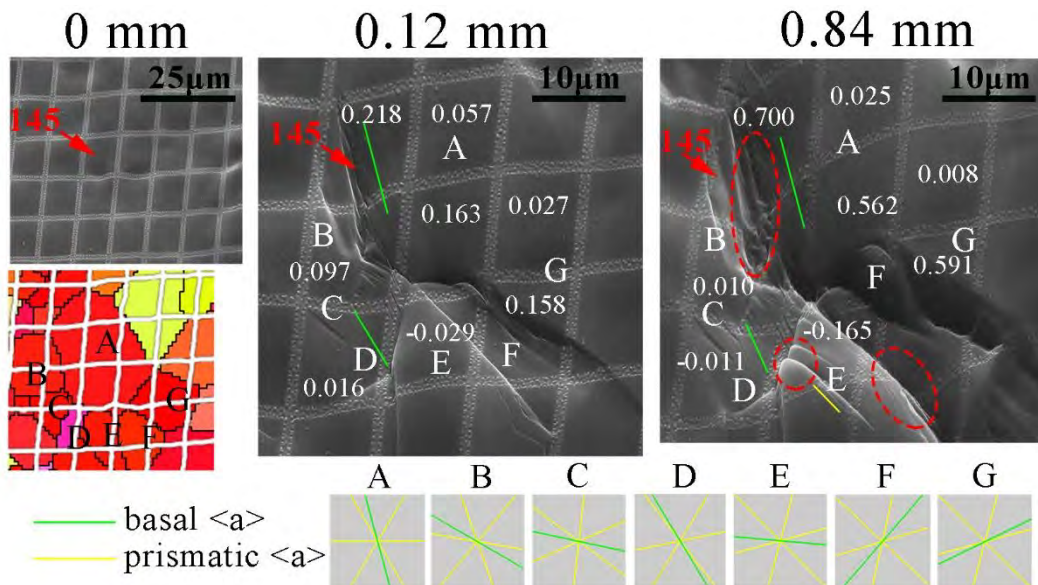


Fig. 9. Microstructural and morphological evolutions of a region in DBs with increasing dome height. Distorted grains are highlighted using red dotted ellipse. The white numbers are the corresponding strains of the grids with corresponding dome height and the number of special grids is also indicated by arrows (similarly hereinafter).

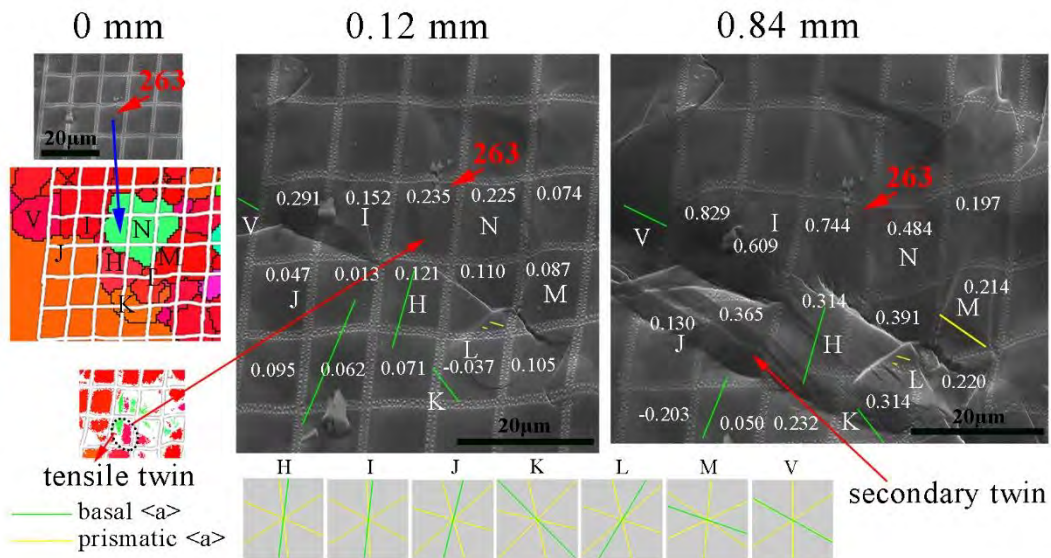


Fig.10. Microstructural and morphological evolutions of a region in DBs including tensile twins and secondary twins with increasing dome height to 0.84 mm.

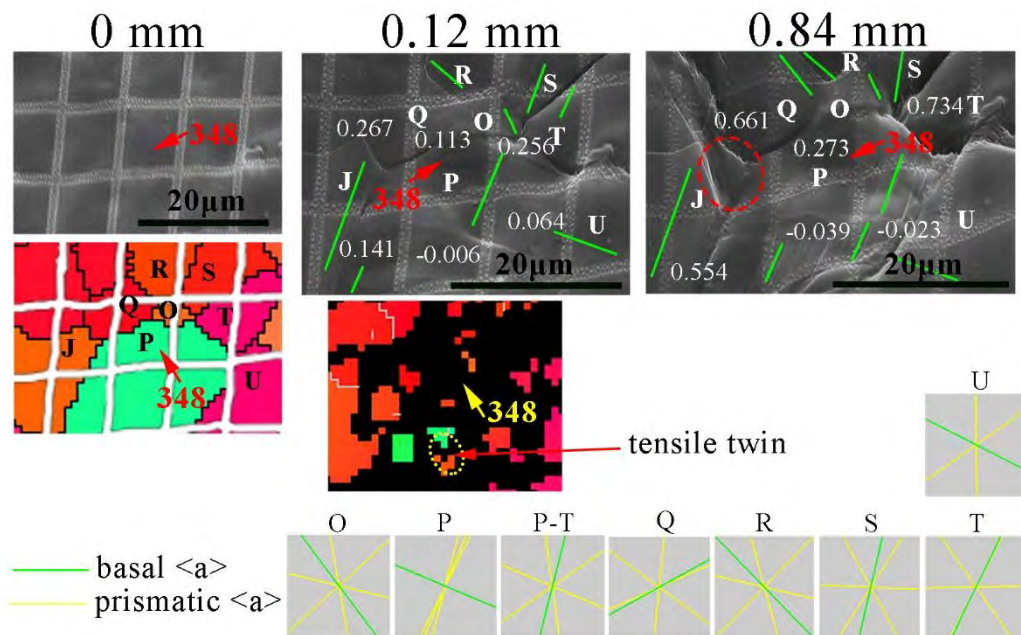


Fig. 11. Microstructural and morphological evolutions of a region in DBs including tensile twins with increasing dome height. Distorted grains are highlighted using dotted ellipse.

Tab. 1 Statistical results of SFs and  $m'$  of grains in Fig. 9.

	SF	$m'$					
		B	C	D	E	F	G
A <i>basal &lt;a&gt;</i>	0.18	<b><i>0.92*</i></b>	<b><i>0.89*</i></b>	0.61	0.27	<b><i>0.94*</i></b>	<b><i>0.95*</i></b>
B <i>basal &lt;a&gt;</i>	<b><i>0.18*</i></b>		<b><i>0.89*</i></b>				
C <i>basal &lt;a&gt;</i>	<b><i>0.08*</i></b>			<b><i>0.74*</i></b>			
D <i>basal &lt;a&gt;</i>	0.45				0.53*		
E <i>prismatic &lt;a&gt;</i>	0.01					<b><i>0.13*</i></b>	
F <i>basal &lt;a&gt;</i>	<b><i>0.17*</i></b>						<b><i>0.99*</i></b>
G <i>basal &lt;a&gt;</i>	<b><i>0.03*</i></b>						

\*As no slip traces are observed in grain B, C, F and G, we use their basal <a> slips to calculate responding SFs and  $m'$  and their results are highlighted using bold italics as a reference since they are not activated (the same below).

Tab. 2 Statistical results of SFs and  $m'$  of grains in Fig. 10

	SF	$m'$					
		I	J	K	L	M	N
H basal $\langle a \rangle$	0.36	0.83*	0.98	0.93	0.17		0.73
I basal $\langle a \rangle$	0.13*		0.83*				0.46*
J basal $\langle a \rangle$	0.36			0.78			
K basal $\langle a \rangle$	0.36				0.30		
L prismatic $\langle a \rangle$	0.02					0.88	
M prismatic $\langle a \rangle$	0.007						0.47
N tensile twin	0.42						
V basal $\langle a \rangle$	0.27	0.95*	0.82				

Tab. 3 Statistical results of SFs and  $m'$  of grains in Fig. 11

	SF	$m'$						
		P	J	Q	R	S	T	U
O basal $\langle a \rangle$	0.41	0.70		0.15		0.01	0.02	
P tensile twin	0.42		0.46	0.32			0.38	0.78
J basal $\langle a \rangle$	0.35			0.90				
Q basal $\langle a \rangle$	0.15				0.89			
R basal $\langle a \rangle$	0.25					0.95		
S basal $\langle a \rangle$	0.20						0.82	
T basal $\langle a \rangle$	0.31							0.77
U basal $\langle a \rangle$	0.32							

Tab. 4 Number of grains in which slip traces appear with different dome height.

	0.12 mm	0.36 mm	0.84 mm
Basal <a>	60	81	85
Prismatic <a>	2	5	8

## Reference

- [1] T.B. Abbott, Magnesium: Industrial and Research Developments Over the Last 15 Years, *Corrosion-Us* 71(2) (2015) 120-127.
- [2] Q.H. Wang, J.F. Song, B. Jiang, A.T. Tang, Y.F. Chai, T.H. Yang, G.S. Huang, F.S. Pan, An investigation on microstructure, texture and formability of AZ31 sheet processed by asymmetric porthole die extrusion, *Mat Sci Eng a-Struct* 720 (2018) 85-97.
- [3] W.J. Joost, P.E. Krajewski, Towards magnesium alloys for high-volume automotive applications, *Scripta Materialia* 128 (2017) 107-112.
- [4] M. Yeganeh, N. Mohammadi, Superhydrophobic surface of Mg alloys: A review, *J Magnes Alloy* 6(1) (2018) 59-70.
- [5] S.H. You, Y.D. Huang, K.U. Kainer, N. Hort, Recent research and developments on wrought magnesium alloys, *J Magnes Alloy* 5(3) (2017) 239-253.
- [6] L.Z. Liu, X.H. Chen, F.S. Pan, A.T. Tang, X.L. Wang, J. Liu, S.Y. Gao, Microstructure, texture, mechanical properties and electromagnetic shielding effectiveness of Mg-Zn-Zr-Ce alloys, *Mat Sci Eng a-Struct* 669 (2016) 259-268.
- [7] W.H. Liu, X. Liu, C.P. Tang, W. Yao, Y. Xiao, X.H. Liu, Microstructure and texture evolution in LZ91 magnesium alloy during cold rolling, *J Magnes Alloy* 6(1) (2018) 77-82.
- [8] J. Kim, H. Ryou, D. Kim, D. Kim, W. Lee, S.H. Hong, K. Chung, Constitutive law for AZ31B Mg alloy sheets and finite element simulation for three-point bending, *Int J Mech Sci* 50(10-11) (2008) 1510-1518.
- [9] J.H. Zhang, S.J. Liu, R.Z. Wu, L.G. Hou, M.L. Zhang, Recent developments in high-strength Mg-RE-based alloys: Focusing on Mg-Gd and Mg-Y systems, *J Magnes Alloy* 6(3) (2018) 277-291.
- [10] L.L.C. Catorceno, H.F.G. de Abreu, A.F. Padilha, Effects of cold and warm cross-rolling on microstructure and texture evolution of AZ31B magnesium alloy sheet, *J Magnes Alloy* 6(2) (2018) 121-133.
- [11] M.H. Yoo, Slip, Twinning, and Fracture in Hexagonal Close-Packed Metals, *Metall Trans A* 12(3) (1981) 409-418.
- [12] K. Hantzsche, J. Bohlen, J. Wendt, K.U. Kainer, S.B. Yi, D. Letzig, Effect of rare earth additions on microstructure and texture development of magnesium alloy sheets, *Scripta Materialia* 63(7) (2010) 725-730.
- [13] R.E. Reedhill, W.D. Robertson, Additional Modes of Deformation Twinning in Magnesium, *Acta Metall Mater* 5(12) (1957) 717-727.
- [14] Z. Keshavarz, M.R. Barnett, EBSD analysis of deformation modes in Mg-3Al-1Zn, *Scripta Materialia* 55(10) (2006) 915-918.
- [15] Y. Chino, K. Kimura, M. Mabuchi, Deformation characteristics at room temperature under biaxial tensile stress in textured AZ31 Mg alloy sheets, *Acta Mater* 57(5) (2009) 1476-1485.
- [16] M.R. Barnett, A rationale for the strong dependence of mechanical twinning on grain size, *Scripta Materialia* 59(7) (2008) 696-698.
- [17] C.M. Cepeda-Jimenez, J.M. Molina-Aldareguia, M.T. Perez-Prado, Effect of grain size on slip activity in pure magnesium polycrystals, *Acta Mater* 84 (2015)

443-456.

- [18] Q. Yu, L. Qi, R.K. Mishra, J. Li, A.M. Minor, Reducing deformation anisotropy to achieve ultrahigh strength and ductility in Mg at the nanoscale, *P Natl Acad Sci USA* 110(33) (2013) 13289-13293.
- [19] T. Al-Samman, G. Gottstein, Room temperature formability of a magnesium AZ31 alloy: Examining the role of texture on the deformation mechanisms, *Mat Sci Eng a-Struct* 488(1-2) (2008) 406-414.
- [20] H.L. Kim, W.K. Bang, Y.W. Chang, Effect of initial texture on deformation behavior of AZ31 magnesium alloy sheets under biaxial loading, *Mat Sci Eng a-Struct* 552 (2012) 245-251.
- [21] Y. Chino, K. Sassa, A. Kamiya, M. Mabuchi, Enhanced formability at elevated temperature of a cross-rolled magnesium alloy sheet, *Mat Sci Eng a-Struct* 441(1-2) (2006) 349-356.
- [22] X.S. Huang, K. Suzuki, Y. Chino, Influences of initial texture on microstructure and stretch formability of Mg-3Al-1Zn alloy sheet obtained by a combination of high temperature and subsequent warm rolling, *Scripta Materialia* 63(4) (2010) 395-398.
- [23] X.S. Huang, K. Suzuki, Y. Chino, M. Mabuchi, Improvement of stretch formability of Mg-3Al-1Zn alloy sheet by high temperature rolling at finishing pass, *Journal of Alloys and Compounds* 509(28) (2011) 7579-7584.
- [24] Y. Chino, M. Mabuchi, Enhanced stretch formability of Mg-Al-Zn alloy sheets rolled at high temperature (723 K), *Scripta Materialia* 60(6) (2009) 447-450.
- [25] A. Vinogradov, V.N. Serebryany, S.V. Dobatkin, *Tailoring Microstructure and Properties of Fine Grained Magnesium Alloys by Severe Plastic Deformation*, *Adv Eng Mater* 20(4) (2018).
- [26] B.C. Suh, J.H. Kim, J.H. Bae, J.H. Hwang, M.S. Shim, N.J. Kim, Effect of Sn addition on the microstructure and deformation behavior of Mg-3Al alloy, *Acta Materialia* 124 (2017) 268-279.
- [27] B.C. Suh, J.H. Kim, J.H. Hwang, M.S. Shim, N.J. Kim, Twinning-mediated formability in Mg alloys, *Sci Rep-Uk* 6 (2016).
- [28] A. Imandoust, C.D. Barrett, T. Al-Samman, K.A. Inal, H. El Kadiri, A review on the effect of rare-earth elements on texture evolution during processing of magnesium alloys, *J Mater Sci* 52(1) (2017) 1-29.
- [29] T. Al-Samman, X. Li, Sheet texture modification in magnesium-based alloys by selective rare earth alloying, *Mat Sci Eng a-Struct* 528(10-11) (2011) 3809-3822.
- [30] V. Herrera-Solaz, J. LLorca, E. Dogan, I. Karaman, J. Segurado, An inverse optimization strategy to determine single crystal mechanical behavior from polycrystal tests: Application to AZ31 Mg alloy, *International Journal of Plasticity* 57 (2014) 1-15.
- [31] V. Herrera-Solaz, R. Hidalgo-Manrique, M.T. Perez-Prado, D. Letzig, J. Llorca, J. Segurado, Effect of rare earth additions on the critical resolved shear stresses of magnesium alloys, *Mater Lett* 128 (2014) 199-203.
- [32] A. Imandoust, C.D. Barrett, H. El Kadiri, Effect of rare earth addition on  $\{10\bar{1}0\}$  twinning induced hardening in magnesium, *Mat Sci Eng a-Struct* 720 (2018) 225-230.

- [33] P. Hidalgo-Manrique, J.D. Robson, M.T. Perez-Prado, Precipitation strengthening and reversed yield stress asymmetry in Mg alloys containing rare-earth elements: A quantitative study, *Acta Materialia* 124 (2017) 456-467.
- [34] B.-C. Suh, J.H. Kim, J.H. Bae, J.H. Hwang, M.-S. Shim, N.J. Kim, Effect of Sn addition on the microstructure and deformation behavior of Mg-3Al alloy, *Acta Materialia* 124 (2017) 268-279.
- [35] T. Hama, H. Takuda, Crystal plasticity finite-element simulation of work-hardening behavior in a magnesium alloy sheet under biaxial tension, *Computational Materials Science* 51(1) (2012) 156-164.
- [36] S.J. Park, H.C. Jung, K.S. Shin, Analysis of the solidification and deformation behaviors of twin roll cast Mg-6Al-X alloys, *Met Mater Int* 22(6) (2016) 1055-1064.
- [37] Y. Yu, M. Wan, X.D. Wu, X.B. Zhou, Design of a cruciform biaxial tensile specimen for limit strain analysis by FEM, *Journal of Materials Processing Technology* 123(1) (2002) 67-70.
- [38] M. Geiger, W. Hussnatter, M. Merklein, Specimen for a novel concept of the biaxial tension test, *Journal of Materials Processing Technology* 167(2-3) (2005) 177-183.
- [39] C.J. Boehlert, Z. Chen, I. Gutierrez-Urrutia, J. Llorca, M.T. Perez-Prado, In situ analysis of the tensile and tensile-creep deformation mechanisms in rolled AZ31, *Acta Materialia* 60(4) (2012) 1889-1904.
- [40] D.F. Shi, T.M. Liu, T.Y. Wang, D.W. Hou, S.Q. Zhao, S. Hussain, {10-12} Twins across twin boundaries traced by in situ EBSD, *Journal of Alloys and Compounds* 690 (2017) 699-706.
- [41] C.C. Tasan, J.P.M. Hoefnagels, M. Diehl, D. Yan, F. Roters, D. Raabe, Strain localization and damage in dual phase steels investigated by coupled in-situ deformation experiments and crystal plasticity simulations, *International Journal of Plasticity* 63 (2014) 198-210.
- [42] A. Chakkedath, C. Boehlert, D. Hernandez, J. Bohlen, S.B. Yi, D. Letzig, In-Situ Ebsd Technique Characterizes Microstructure Evolution of Magnesium Alloy, *Adv Mater Process* 174(6) (2016) 19-21.
- [43] C. Mo, A. Kontsos, Twinning contributions to strain localizations in magnesium alloys, *Mat Sci Eng a-Struct* 722 (2018) 206-215.
- [44] Y.J. Cui, Y.P. Li, Z.C. Wang, Q. Lei, Y. Koizumi, A. Chiba, Regulating twin boundary mobility by annealing in magnesium and its alloys, *International Journal of Plasticity* 99 (2017) 1-18.
- [45] B.L. Wu, G.S. Duan, X.H. Du, L.H. Song, Y.D. Zhang, M.J. Philippe, C. Esling, In situ investigation of extension twinning-detwinning and its effect on the mechanical behavior of AZ31B magnesium alloy, *Materials & Design* 132 (2017) 57-65.
- [46] A. Vinogradov, A.V. Danyuk, D.L. Merson, I.S. Yasnikov, Probing elementary dislocation mechanisms of local plastic deformation by the advanced acoustic emission technique, *Scripta Mater* 151 (2018) 53-56.
- [47] K. Mathis, K. Horvath, G. Farkas, H. Choe, K.S. Shin, A. Vinogradov, Investigation of the Microstructure Evolution and Deformation Mechanisms of a

**Mg-Zn-Zr-RE Twin-Roll-Cast Magnesium Sheet by In-Situ Experimental Techniques, *Materials* 11(2) (2018).**

- [48] J. Sun, L. Jin, J. Dong, W.J. Ding, A.A. Luo, Microscopic deformation compatibility during monotonic loading in a Mg-Gd-Y alloy, *Materials Characterization* 119 (2016) 195-199.
- [49] D. Raabe, M. Sachtleber, Z. Zhao, F. Roters, S. Zaeferrer, Micromechanical and macromechanical effects in grain scale polycrystal plasticity experimentation and simulation, *Acta Materialia* 49(17) (2001) 3433-3441.
- [50] F. Delaire, J.L. Raphanel, C. Rey, Plastic heterogeneities of a copper multicrystal deformed in uniaxial tension: Experimental study and finite element simulations, *Acta Materialia* 48(5) (2000) 1075-1087.
- [51] D.B. Xia, G.S. Huang, Q.Y. Deng, B. Jiang, S.S. Liu, F.S. Pan, Influence of stress state on microstructure evolution of AZ31 Mg alloy rolled sheet during deformation at room temperature, *Mat Sci Eng a-Struct* 715 (2018) 379-388.
- [52] M.R. Barnett, Z. Keshavarz, M.D. Nave, Microstructural features of rolled Mg-M-1Zn, *Metall Mater Trans A* 36a(7) (2005) 1697-1704.
- [53] Y.B. Chun, C.H.J. Davies, Texture effects on development of shear bands in rolled AZ31 alloy, *Mat Sci Eng a-Struct* 556 (2012) 253-259.
- [54] F. Kabirian, A.S. Khan, T. Gnäupel-Herlod, Visco-plastic modeling of mechanical responses and texture evolution in extruded AZ31 magnesium alloy for various loading conditions, *International Journal of Plasticity* 68 (2015) 1-20.
- [55] R. Pippan, S. Wurster, D. Kiener, **Fracture mechanics of micro samples: Fundamental considerations, *Mater Design* 159 (2018) 252-267.**
- [56] Z.R. Zeng, M.Z. Bian, S.W. Xu, C.H.J. Davies, N. Birbilis, J.F. Nie, Effects of dilute additions of Zn and Ca on ductility of magnesium alloy sheet, *Mat Sci Eng a-Struct* 674 (2016) 459-471.
- [57] T. Obara, H. Yoshinga, S. Morozumi, [112̄]<sub>2</sub>(11̄)<sub>23</sub> Slip System in Magnesium, *Acta Metall Mater* 21(7) (1973) 845-853.
- [58] J. Koike, R. Ohyama, Geometrical criterion for the activation of prismatic slip in AZ61 Mg alloy sheets deformed at room temperature, *Acta Materialia* 53(7) (2005) 1963-1972.
- [59] Z. Keshavarz, M.R. Barnett, In-situ investigation of twinning behaviour in Mg-3Al-1Zn, *Magnesium Technology 2005* (2005) 171-175.
- [60] M.R. Barnett, M.D. Nave, A. Ghaderi, Yield point elongation due to twinning in a magnesium alloy, *Acta Materialia* 60(4) (2012) 1433-1443.
- [61] K. Hagihara, T. Mayama, M. Honnami, M. Yamasaki, H. Izuno, T. Okamoto, T. Ohashi, T. Nakano, Y. Kawamura, Orientation dependence of the deformation kink band formation behavior in Zn single crystal, *International Journal of Plasticity* 77 (2016) 174-191.
- [62] H.Y. Gao, K. Ikeda, T. Morikawa, K. Higashida, H. Nakashima, Analysis of kink boundaries in deformed synchronized long-period stacking ordered magnesium alloys, *Mater Lett* 146 (2015) 30-33.
- [63] B.L. Xi, G. Fang, S.W. Xu, Multiscale mechanical behavior and microstructure evolution of extruded magnesium alloy sheets: Experimental and crystal plasticity

analysis, Mater Charact 135 (2018) 115-123.

[64] L.Y. Zhao, Y.C. Xin, Y. Wu, Q. Liu, The texture dependence of strength in slip and twinning predominant deformations of Mg-3Al-1Zn alloy, Mat Sci Eng a-Struct 717 (2018) 34-40.

[65] D.D. Yin, Q.D. Wang, C.J. Boehlert, Z. Chen, H.M. Li, R.K. Mishra, A. Chakkedath, In-Situ Study of the Tensile Deformation and Fracture Modes in Peak-Aged Cast Mg-11Y-5Gd-2Zn-0.5Zr (Weight Percent), Metallurgical and Materials Transactions A 47(12) (2016) 6438-6452.

[66] D. Steglich, Y. Jeong, M.O. Andar, T. Kuwabara, Biaxial deformation behaviour of AZ31 magnesium alloy: Crystal-plasticity-based prediction and experimental validation, Int J Solids Struct 49(25) (2012) 3551-3561.

[67] J.Y. Min, T.B. Stoughton, J.E. Carsley, B.E. Carlson, J.P. Lin, X.L. Gao, Accurate characterization of biaxial stress-strain response of sheet metal from bulge testing, International Journal of Plasticity 94 (2017) 192-213.